Bioactive Materials 28 (2023) 132–154

Contents lists available at ScienceDirect

Bioactive Materials

journal homepage: www.keaipublishing.com/en/journals/bioactive-materials

In vitro and in vivo degradation behavior of Mg-0.45Zn-0.45Ca (ZX00) screws for orthopedic applications

Diana C. Martinez [a], Anna Dobkowska [a], Romy Marek [b], Hanna Ćwieka [c], Jakub Jaroszewicz [a], Tomasz Płociński [a], Črtomir Donik [d], Heike Helmholz [c], Bérengère Luthringer-Feyerabend [c], Berit Zeller-Plumhoff [c], Regine Willumeit-Römer [c], Wojciech Święszkowski [a,*]

[a] Biomaterials Group, Materials Design Division, Faculty of Materials Science and Engineering, Warsaw University of Technology, Wołoska 141, 02-507, Warsaw, Poland
[b] Department of Orthopedics and Traumatology, Medical University of Graz, Auenbruggerplatz 5, 8036, Graz, Austria
[c] Institute of Metallic Biomaterials, Helmholtz-Zentrum Hereon GmbH, 21502, Geesthacht, Germany
[d] Department of Physics and Chemistry of Materials, Institute of Metals and Technology, University of Ljubljana, Lepi Pot 11, SI-1000, Ljubljana, Slovenia

ARTICLE INFO

Keywords:
Magnesium alloys
Biodegradable implants
Microstructure
Electron microscopy
Corrosion layers

ABSTRACT

Magnesium (Mg) alloys have become a potential material for orthopedic implants due to their unnecessary implant removal, biocompatibility, and mechanical integrity until fracture healing. This study examined the *in vitro* and *in vivo* degradation of an Mg fixation screw composed of Mg-0.45Zn-0.45Ca (ZX00, in wt.%). With ZX00 human-sized implants, *in vitro* immersion tests up to 28 days under physiological conditions, along with electrochemical measurements were performed for the first time. In addition, ZX00 screws were implanted in the diaphysis of sheep for 6, 12, and 24 weeks to assess the degradation and biocompatibility of the screws *in vivo*. Using scanning electron microscopy (SEM) coupled with energy dispersive X-ray spectroscopy (EDX), micro-computed tomography (μCT), X-ray photoelectron spectroscopy (XPS), and histology, the surface and cross-sectional morphologies of the corrosion layers formed, as well as the bone-corrosion-layer-implant interfaces, were analyzed. Our findings from *in vivo* testing demonstrated that ZX00 alloy promotes bone healing and the formation of new bone in direct contact with the corrosion products. In addition, the same elemental composition of corrosion products was observed for *in vitro* and *in vivo* experiments; however, their elemental distribution and thicknesses differ depending on the implant location. Our findings suggest that the corrosion resistance was microstructure-dependent. The head zone was the least corrosion-resistant, indicating that the production procedure could impact the corrosion performance of the implant. In spite of this, the formation of new bone and no adverse effects on the surrounding tissues demonstrated that the ZX00 is a suitable Mg-based alloy for temporary bone implants.

1. Introduction

In orthopedic surgery, permanent or temporary implants are used for realignment and fixation to ensure adequate bone healing. Permanent implants, such as the ankle, knee, wrist, or hip implants, will ideally function in the human body for the patient's life [1]. Temporary orthopedic implants, such as pins, wires, screws, or plates, are used to repair fractured bones and are only meant to be used for an adequate time [2]. Usually, metallic orthopedic implants made from Co-based alloys, stainless steel, and Ti and its alloys are considered the gold standard metals for the internal fixation [3]. However, toxic metallic ion release, periprosthetic infection, and stress shielding effects are permanent metallic implant-related complications [3–6].

These drawbacks of permanent implants could inhibit the bone formation or bone resorption processes and necessitate a second surgery to retrieve or remove them after the bone has healed [7]. On the other hand, due to its similar mechanical properties close to the bone, such as elastic modulus and density, Mg and its alloys are promising biodegradable materials [3,8–16]. Furthermore, as a material for orthopedic applications, Mg-based devices have shown osteoinductive and osteoconductive effects, substantially high mineral apposition rates, and enhanced bone mass around Mg-implants [17,18]. Nevertheless, one

Peer review under responsibility of KeAi Communications Co., Ltd.
* Corresponding author.
E-mail address: wojciech.swieszkowski@pw.edu.pl (W. Święszkowski).

https://doi.org/10.1016/j.bioactmat.2023.05.004
Received 28 February 2023; Received in revised form 26 April 2023; Accepted 9 May 2023

major obstacle that limits the application of Mg-based implants is its high corrosion rate, often leading to premature implant failure before bone tissue healing is completed [3,14,19–25].

Improving the corrosion resistance of Mg-based alloys is commonly considered an issue by researchers investigating biomaterials [26,27]. Purifying, alloying, coating, and surface treatments are different approaches that can decrease the corrosion activity of Mg-based materials [28]. It is worth noting that alloying elements not only improve biocompatibility and control of the degradation behavior but can also improve the mechanical properties of the material and introduce another biological function such as antibacterial effects (Ag) or further cellular processes (Zn, Ca) [24,29–32]. Studies show that resistance to general and pitting corrosion of Mg alloys is improved by adding Ca [9,23,33,34]. Zn also enhances the corrosion resistance of Mg alloys via a solid hardening mechanism and may reduce hydrogen evolution during the degradation [8,28,29,34,35]. Moreover, Zn is essential for numerous biological functions in the human body, such as stimulation of new bone formation, preservation of bone mass, signal transmission, apoptosis regulation, and gene expression [36]. However, the high concentration of Zn can cause microporosity during solidification and increase the susceptibility to corrosion attack [24,37,38].

Recent preclinical studies [17,32,39–41] have demonstrated that the alloying system Mg–Zn–Ca (ZX alloys) is biologically safe and promotes osseointegration. Jang et al. [42] examined the corrosion behavior of Mg–Zn–Ca alloys in subcutaneous mouse models for 60 days. They observed that with the increasing Zn concentration, the degradation rate of the materials accelerated. Using micro-computed tomography (μCT) analysis, Kraus et al. [17] investigated the degradation behavior of ZX50 (Mg–5Zn-0.25Ca in wt.%) and WZ21 (Mg–1Zn–2Y in wt.%) pins. Although the results demonstrated that ZX50 degrades more rapidly with high hydrogen gas formation, an improvement in bone formation around the implant was observed. Grün et al. [32] studied the degradation behavior of ZX00 (Mg-0.45Zn-0.45Ca in wt.%) alloy using models of both small and large animals. After 6, 12 and 24 weeks of *in vivo* implantation the alloy degraded slowly and uniformly, with no adverse effect on bone formation and in-growth. Holweg et al. [39] examined the degradation performance of ZX00 screws for fracture stabilization in a sheep model, and they demonstrated that the osteotomies completely consolidated after 12 weeks. In the femur of juvenile rats, Cihova et al. [40] implanted ZX10 (Mg–1Zn-0.3Ca in wt.%) and ZX20 Mg-1.5Zn-0.25Ca in wt.%) pins, and it demonstrated that ZX10 degraded at a slower rate when compared to ZX20. Mao et al. [41] observed a slow degradation rate after 12 weeks when Mg–2Zn-0.05Ca rods were implanted in femoral condyles of rabbits with severe localized corrosion between 12 and 16 weeks, without accumulation of corrosion products in the surrounding tissues. Sommer et al. [43] studied the degradation of ZX00 pins after 4, 8 and 12 weeks of implantation in juvenile, old, and osteoporotic rats. Compared to young and aged rats, the osteoporotic rats exhibited accelerated degradation and increased gas evolution. After 24 weeks of implantation of ZX00 pins in rats, Okutan et al. [44], observed homogeneous degradation along with increased gas accumulation and superior new bone tissue formation. Marek et al. [45] also investigated the degradation behavior of ZX00 screws at various implant locations. According to their findings, the cortical bone thickness was greater around ZX00 screws than Ti screws, which showed low bone-to-implant contact (BIC) values. Similarly, they implanted trans-epiphyseal ZX00 nails in juvenile sheep, demonstrating no deleterious influence on the longitudinal bone growth, despite bone-structure alterations observed in the initial phase of ZX00 nail degradation [46]. Han et al. [47] implanted Mg5Ca1Zn pins in the femoral condyle of rats and observed accelerated bone healing due to the release of anabolic metallic ions into the adjacent tissues, which stimulated the growth of blood vessels and actively recruit osteoprogenitors cells.

One of the most critical problems regarding Mg–Zn–Ca alloys used in biomedicine is the precipitation-dependent corrosion of those alloys. Hofstetter et al. [24] investigated *in vitro* and *in vivo* corrosion behavior of conventional purity and ultrahigh-purity Mg–5Zn-0.3Ca (ZX50) Mg pins and found that a reduction in the impurity level to trace amounts decreased the alloy's degradation rate. Cihova et al. [40] compared Mg–1Zn-0.3Ca (ZX10) and Mg-1.5Zn-0.25Ca (ZX20) in terms of micro-galvanic corrosion, where various phases formed micro- or nano-galvanic couple with Mg matrix. They stated that the large cathode-to-anode ratio of μm-sized Mg-matrix grains and nanometric Mg_2Ca-type intermetallic particles (IMPs) expectedly caused the rapid dissolution of the latter in the ZX10 alloy. Nevertheless, the corrosion of ZX10 screws can be controlled, and the continuous degradation of the biomimicking calcification matrix initiates the bone formation process [48].

The extensive research on Mg as an absorbable metal has evolved into translational research. There have been clinical trials with Mg-based implants for orthopedic applications, and pure Mg, Mg–Ca–Zn, and Mg-RE screws are currently in clinical use [11,48–55]. Nevertheless, despite the fact that Mg implants can be used as absorbable metals for orthopedic applications, a 13% complicate rate [56] has been reported, including swelling and moderate hyperemia [57,58], femoral head collapse [50], resorption cysts [59], postoperative infection and pain [56]. Hence, it is meaningful to explore the causes of such clinical complications and how tailor de corrosion resistance of Mg implant to overcome these challenges.

Although the behavior of ZX alloys has been several times investigated under *in vitro* and *in vivo* conditions, there is a significant lack of information on the corrosion processes and changes in thickness and composition of the corrosion products resulting in degradation of Mg-0.45Zn-0.45Ca (ZX00) screws under physiological conditions. It is crucial to investigate the corrosion layer formed during Mg degradation as the formation of this layer might be modified and change during the implant degradation with some ions released and absorbed earlier than others [60], and as a consequence, various degradation could be observed [61].

Previous studies of the ZX00 alloy have examined the microstructure and estimated the corrosion rate *in vitro* using simple samples (i.e. rods), while *in vivo* studies have been conducted using screw-shaped implants [39,40,62]. The fabrication procedures used for Mg-based implants have a direct influence on their properties and performance in the biological environment [63,64]. Marco et al. [65] observed distinct degradation of pure Mg, Mg-10Gd and Mg–2Ag alloys *in vitro and in vivo*. According to their findings, the increased corrosion rate observed *in vitro* may be due to different immersion solutions employed or the presence of impurities in the alloys, but it may also be the result of different processing routes, as *in vitro* specimens were disc-shaped while *in vivo* specimens were pin-shaped, with larger grain size in the discs compared to the pins. Similarly, Liu et al. [66] found that differences in grain size and texture of pure Mg and AZ31 formed during different manufacturing processes may result in different local interactions with biomolecules such as proteins under physiological conditions, further contributing to the different immune responses. This was observed when pure Mg and AZ31 pins were implanted in the femoral shaft of rats.

In addition to the manufacturing procedures, the local tissue metabolism at the implantation site also influences the corrosion of Mg implants. The interface between a surgical implant and the adjacent tissues is characterized by complex and dynamic mechanical and biological interactions (immune and inflammatory response as well as bone healing processes [67]) between the implant and surrounding tissues [68,69]. These interfaces between tissues (bone, cartilage, tendon, ligament, muscle and soft tissues) and Mg implants are of crucial importance; and influence the corrosion performance of Mg-based devices and the healing and remodeling potential of tissues [70]. Understanding the complex biological interactions between Mg implants and adjacent tissues is essential for the target-oriented implant development processes of Mg-based devices taking into account the implantation sites used in clinics [71]. Consequently, it is still necessary to investigate the

corrosion performance of Mg–Zn–Ca alloys and the influence of the processing routes in order to comprehend their degradation and interactions with the physiological environments to which the alloy is exposed. Hence, this study investigates the degradation behavior of low-alloyed ZX00 screws with the same geometry and dimensions under physiological conditions (*in vitro* and *in vivo*) and, for the first time, characterizes the subsequent corrosion products at different screw zones, with an emphasis on the impact that the manufacturing process may have on the corrosion performance at various regions of the screw: the head, the valley, and the tip.

2. Material and methods

2.1. The fabrication process of the screw

Custom-made (not commercially available) screws were manufactured by Ernst Wittner GmbH, Wien, Austria, from extruded rods produced at ETH Zürich in collaboration with Cavis AG. Briefly, the screws were fabricated from the ZX00 alloy (Mg-0.45Zn-0.45Ca) which was made from pure Mg (99.9999 wt%) alloyed with Ca (99.95 wt%) and Zn (99.9999 wt%), and subsequently extruded to the shape of rods with 6 mm in diameter. The extrusion and homogenization process is further described in Ref. [39]. The thread and the head of the screws were computer-turned (using a computer numerical control machine, CNC), and the head's Torx was drily milled without using cooling oil to reduce the risk of corrosion attack and contamination. The screws were ultrasonically cleaned in acetone, air-dried and gamma sterilized at 25 kGy γ-radiation dose. As shown in Fig. S1, the screws were fabricated with a length of 16 mm, an outer diameter of 3.5 mm, and a head diameter of 5.7 mm.

2.2. Microstructure characterization

The surface morphology of the as-received sterilized ZX00 screws was analyzed using a stereomicroscope (Olympus SZ61, Japan) and scanning electron microscopy (SEM, Hitachi, SU-8000, Japan) equipped with an energy dispersive X-ray detector (EDX, UltraDry EDS Detector, Thermo Scientific™). The chemical composition of the as-manufactured screw determined by EDX is presented in Table S1. The surface roughness was determined by analyzing three random areas of 100 μm × 100 μm per screw using a confocal laser scanning microscope (CLSM, Keyence, VK-1000, Japan). The phase composition of the screws was determined using X-ray diffraction (XRD, Bruker D8 Advance) operated at 40 kV and 40 mA with Cu-Kα radiation. The results were recorded by stepwise scanning 2θ from 10° to 120°, with a step size of 0.02° and a count time of 10 s per step. The microstructures on the surface perpendicular to the extrusion direction were observed using an SEM (Hitachi, SU70, Japan) after ion milling in an Ar + beam (Hitachi, IM 4000, Japan). Crystallographic orientations and distribution of grain sizes were calculated based on the results obtained from the electron backscattered diffraction (EBSD) performed on the SEM SU70 equipped with a Bruker EBSD detector. The EBSD scans were conducted with a step size of 0.1 μm. The crystallographic orientations of grains are shown as inverse pole figure (IPF) maps where various colors distinguish an orientation of a given sample direction in a crystal frame. Grain boundary characterizations are also shown. If the angle between two neighboring grains was distorted by more than 15°, then the angle between those grains was described as a high-angle grain boundary (HAGB). When the grains were misoriented by less than 15°, a low-angle grain boundary (LAGB) was created between those grains. Additionally, Kernel average misorientation maps calculated for 5th nearest neighbors are depicted.

2.3. In vitro studies

2.3.1. Immersion tests

Thirty screws were entirely immersed in α-minimum essential medium (α-MEM; Life Technologies, Germany), supplemented with 10% fetal bovine serum (FBS) (Gibco, Life Technologies, Germany) and 1% penicillin/streptomycin (100 units/mL penicillin and 100 μg/mL streptomycin P/S; Invitrogen, Germany) for 3, 6, 14, 21, and 28 days, respectively (n = 6/time point). Sterilized 12-well culture plates (Greiner Bio-One, Germany) were used to place one ZX00 screw per well. Each sample was immersed in 2 mL of immersion medium and incubated under cell culture conditions (37 °C, 5% CO_2, 20% O_2 and 95% controlled humidity). Three empty wells filled with immersion medium were used as the control. The immersion medium was changed every 2–3 days. The pH and osmolality of the initial culture medium were recorded using a pH meter (Sentron® SI600, Sentrom Europe BV, Netherlands) with a MiniFET probe and a cryoscopic osmometer (OSMOMAT® auto, Gonotec GmbH, Germany), respectively. The pH and osmolality of the supernatant with and without samples were measured after each cell culture medium change. At the determined time of immersion (3, 6, 14, 21 and 28 days), samples were rinsed with deionized water and ethanol and finally air-dried.

Hydra Medusa Software [72] was used to calculate the fraction of the chemical equilibrium diagrams for each immersion time point based on the ionic concentration of the immersion medium composition (Table S2). The Mg concentration was determined using the calculated the corrosion rate (CR) based on the mass loss measurements to understand the various compounds that could form during the immersion in the solution used for this research throughout the entire pH range.

2.3.2. Corrosion rate calculations after in vitro immersion

To calculate CR based on mass loss measurements, after immersion in the α-MEM medium for the defined time, the corrosion products from the samples (n = 3screws/time point) were chemically removed by samples treatment in fresh chromic acid (180 g/L in distilled water, VWR International, Germany). Equation (1) was used to calculate the CR [73]:

$$CR = (K \times W)/(A \times T \times D) \quad (1)$$

where: K is a constant (8.76×10^4 mm × y^{-1}), W is the mass loss change (g), A is the exposed surface area (cm^2), T is the time of exposure (h), and D is the material density (g × cm^{-3}).

All 3–28 days of data were fitted with linear regression and inserted into an empirical two-parameter Equation (2) [74].

$$h = h_{\infty}.t + h_0 \quad (2)$$

where h is the mean degradation depth in μm, h_{∞} describes the CR of the alloy at higher immersion times, t is the total incubation time in days, and h_0 is the y-intercept describing the degradation depth to initial reactions.

The CR calculated based on the mass loss measurements were compared with CR calculated using microcomputed tomography (μCT, Poenix Nanotom®, GE, Germany). To quantify CR, μCT scans were conducted at 100 keV, 1000 ms exposure time, and 7.5 μm voxel size on three immersed specimens for each designated time. X-AID 2021.2.0. (MITOS, GmbH, Garching, Germany) and Amira-Avizo 9.4.0 (FEI SAS, ThermoScientific, France) software were used for reconstruction and segmentation, respectively. The corrosion rate of the screws was determined using Equation (3) [75]:

$$CR = \frac{V_i - V_r}{A * t} \quad (3)$$

where V_i is the volume of the as-received screw before immersion (mm^3), V_r is the residual volume (mm^3), A is the surface area of the as-received screw before immersion (mm^2), and t is the immersion time

(year). Before immersion tests, the initial volume and surface, the volume and surface area of the original screw were calculated and it was found to be 114.54 mm^3 and 229.53 mm^2, respectively.

2.3.3. Characterization of the screws after in vitro immersion tests

After immersion tests, the macro images of the specimens were taken using an Olympus SZ61 stereomicroscope. Further observations of the corroded screws were done using SEM (Hitachi S3500 N, Japan) in low vacuum mode at 70 Pa. The chemical analyses of the corrosion products were done using an energy-dispersive X-ray spectrometer (EDX, Ultra-Dry EDS Detector, Thermo Scientific™). After each immersion period, changes in the surface area (S_A, mm^2) recorded using μCT were calculated using Equation (4):

$$S_A = A_i - A_d \quad (4)$$

where A_i is the surface area calculated for the specimen after immersion, and A_d is the surface area of the corroded screw after removal of the corrosion layer. Additionally, the reconstructed 3D images of *in vitro* samples with and without corrosion products were shown and compared.

To determine the thickness and chemical composition of the corrosion layers, cross-sectional observations of *in vitro* specimens were performed. The samples were ion milled using IM4000 Hitachi Ion Milling System and subsequently coated with carbon. Then, measurements of the thickness of the corrosion layer were performed using Fiji software [76]. XRD measurements were performed on the immersed screws. However, except for peaks from the substrate phases and strong background noise, no information was obtained from the corroded surfaces. Similar challenges in identifying the phase constituents of the corrosion products have been reported previously [77–79]. Therefore, the chemical composition of the corrosion products formed on the three zones of the screw (head, valleys, tip) after 3 days of *in vitro* immersion were characterized using Versa Probe III AD photoelectron spectroscopy (XPS, PHI, USA) with a monochromatic Al K_α (1486.3 eV) X-ray source. For each measurement, spectra were acquired on a 200 μm analysis spot size with a charge neutralizer turned since the thick, unconducive oxides were present on the surface after the immersion. Survey spectra were measured at a pass energy of 224 eV and a step of 1 eV, while high-resolution XPS spectra were measured at a pass energy of 55 eV and a step of 0.05 eV. For survey spectra, 10 cycles were performed, and for all the HR spectra measurements, at least 15 cycles were done. The XPS spectra were corrected for the possible charging effect using carbon C 1s peak with the binding energy of 284.7 eV. After acquiring the spectra, the data were processed with the CasaXPS with Shirley background subtraction. The accuracy of the binding energy (BE) scale is estimated to be 0.2 eV. High-resolution spectra for Mg 1s, O 1s, C 1s and Ca 2p were analyzed. To remove the top layer of the sample, Ar^+ ion sputtering of the sample was performed. Sputter time was 2 min at 2 kV over a 2 mm × 2 mm area that was centered in the middle of the sample. Zalar rotation was turned on to sputter the sample evenly and to eliminate the ripening effect of the sputtering. Right after sputtering, high-resolution spectra for C 1s, O 1s, Mg 1s and Ca 2p were acquired on a spot area centered in the middle of the sample.

2.3.4. Electrochemical measurements

The corrosion resistance of the tip, the thread and the head of the screws was analyzed using electrochemical methods (open circuit potential, electrochemical impedance spectroscopy (EIS) and potentiodynamic polarization) in phosphate-buffered saline solution (PBS, tablets purchased from Sigma Aldrich). One tablet dissolved in 200 mL of deionized water yields 10 mM phosphate buffer, 2.7 mM potassium chloride, 137 mM sodium chloride, and a pH of 7.4. The electrochemical setup was composed of a platinum (Pt) wire as a counter electrode, silver chloride (Ag/AgCl) as a reference electrode, and the measured sample as the working electrode. Testing was done using potentiostat Gamry Instruments Reference 600+ at 37 °C. First, the open circuit measurements were carried out for 1 h. Afterwards, EIS and potentiodynamic tests were recorded. EIS was carried out at open circuit potential with an AC amplitude of 10 mV over a frequency range from 0.01 Hz to 10 kHz. The potentiodynamic polarization tests were registered from the 0.5 V below open circuit potential (E_{OCP}) to 1.5 V vs E_{OCP} with a scan rate of 1 mV/s. The results were fitted using Gamry Framework™ software 7.8.2. For the electrochemical testing, samples were molded in acrylic resin. The exposed area of the samples was ground using 600-4000-grit SiC papers and subsequently polished with 3 and 1 μm water-free diamond suspensions (glycol-based lubricant was used). To ensure the reproducibility of the results, at least three measurements for each sample were made.

2.4. In vivo animal model

Ethical statement

The large animal trial (Permit number: BMBWF-66.010-0107-V-3b-2019) was approved by the Austrian Federal Ministry for Science and Research and followed the guidelines for the accommodation and care of animals formulated by the European Convention for the protection of vertebrate animals used for experimental and other scientific purposes. The experiment was performed according to the 3R principles (replace, reduce, and refine).

2.4.1. Animal surgical procedure

The *in vivo* degradation behavior of ZX00 screws was evaluated after implantation into the diaphysis of sheep (Ovis aries) over 24 weeks. 3-month-old female lambs were randomly assigned to three groups for observation periods of 6, 12 or 24 weeks (n = 3 per group). The sheep were group-housed at the testing facility (Medical University of Graz) in a sheep-shed with access to the outdoor meadows for one week prior to surgery, to reduce stress and enable environmental acclimation. Food and water were always provided *ad libitum*. All lambs underwent surgeries under sterile clinical conditions and general anesthesia. After shaving and disinfection of the tibiae, three ~2 cm long incisions were made at 3–5 cm distances in the medial diaphyseal area, followed by periosteal dissection down to the bone. Bicortical drilling was performed at each dissected area, using a 2.7 mm drill bit and a 3.5 mm tapper. 18 screws were implanted into the right diaphysis of the animals in a strictly lateral direction to the tibial shaft (Fig. S2). Wounds were closed in layers and disinfected using an iodine solution. Carprofen and buprenorphine were used as postoperative analgesia for four days, while gentamicin and penicillin were administered for infection prophylaxis reasons for five days. Wound checking was performed daily by trained employees for two weeks. Following, the sheep were transferred to an external housing facility, where they were kept on meadows with a shelter with access to hay, food, and water *ad libitum*. Daily inspection concerning behavioral peculiarities (e.g., eating, moving, etc.) was performed by the farmer and at least weekly by a vet. The animals were transferred back to the animal facility for the sacrification which was done by intravenous overdose injection of propofol, ketamine and potassium chloride after 6, 12 or 24 weeks. Finally, one tibia per animal was harvested for further use. Titanium (Ti) screws with similar dimensions were implanted in the left diaphysis of sheep as a control. The comparative analysis between ZX00 and Ti screws has been described in Refs. [45,80]. Therefore, these data are not presented here.

2.4.2. Ex vivo micro-computed tomography data acquisition and analyses

Ex vivo μCT imaging was performed on all harvested tibiae using a Bruker SkyScan 1276 scanning device (Bruker, Germany). An aluminum-copper filter was used with operating voltage and current of 100 kV and 200 mA, respectively. The rotation step size was set to 0.4° at a binned pixel size of 80.2 μm. Nine explants were scanned, three explants per time point. The scanned data was converted into DICOM format and imported to Avizo Fire Software (version 2020.2). For

descriptive analysis, two-dimensional (2D) planes and three-dimensional (3D) reconstructions were assessed using Avizo Fire Software. The radiolucent zones adjacent to the screws were defined as gas bubbles caused by the corrosion of the screws.

2.4.3. Characterization of the corroded surfaces

Following μCT imaging, the diaphysis was cut in the transverse plane with a minimum of 2 cm from the screws. One-half of the screws (n = 9) were used for the characterization of the corroded surfaces, while the other half (n = 9) was used for the SEM/EDX and histological examination of the implant-tissue interface. For the corrosion layers characterization, three ZX00 screws were investigated after 6, 12, and 24 weeks of implantation. To extract the screws from the bone, the cortex of the diaphyses were cut using a Dremel rotatory cutter with a wood blade (SC544). Special care was taken to not cut into the screw or the corrosion layers. Then, the screw implants were carefully removed and fixed in 100% ethanol for 2 h and air-dried for 2h. Specimens were stored under vacuum conditions until microscope analysis. Stereomicroscope, SEM/EDX analysis in a low-vacuum mode (70 Pa) was performed to determine the surface morphology and the chemical composition of the corrosion layers at the head, shaft, and valley regions of the screw. For corrosion morphology analysis at the bone-implant interface, three bone-implant specimens per time point were retrieved and fixed in 70% ethanol at 4 °C for at least five days. Afterwards, bone-implant tissue blocks were dehydrated in ascending grades of alcohol (80%, 96%, and 100%), infiltrated, and embedded in Technovit® 9100 New (Heraeus Kulzer) as described by Willbold et al. [81]. Then, embedded blocks were cut parallel to the longitudinal axis of the screws. The specimens were ground using up to 4000-grit SiC paper and ion milled in an Ar + beam (Hitachi System IM4000).The samples were coated with a 10 nm carbon layer using the Gatan precision etching coating system (PECS, Gatan 682). To determine the thickness and composition of the corrosion layer at different zones of the screws in the cortical bone and intra medullary cavity compartments, cross-sections were observed under SEM equipped with EDX. The distribution of O, Mg, P, and Ca on the cross sections of the corrosion layers were analyzed based on SEM-EDX maps and line scans. EDX point analysis was performed to semi-quantitatively analyze the elemental composition of the corrosion layer on the surface of ZX00 screws and to investigate the atomic ratio of Ca/P in the peri-implant bone regions. Image processing and bone-implant contact (BIC) determination were performed using Fiji image processing software. Mosaic J plugin [82] was used to stitch together backscattered electron (BSE) images to have an overall image of the cross-section of the resin bone-ZX00 screws blocks.

2.4.4. Histological evaluation

After SEM observations and before histological staining, one ZX00 bone-implant embedded block per time point was prepared by cutting along the longitudinal axis of the implant using a laser microtome (TissueSurgeon, LLS ROWIAK LaserLabSolutions) [83]. 10–15 μm sections fixed on glass slides were stained using McNeal staining (Tetrachrome, Toluidine Blue and Basic Fuchsin). The mounted slides were examined under transmitted light using an optical microscope (Nikon Eclipse E600) coupled with a Nikon DS-Fi3 Camera. Whole slide imaging was acquired at 4x/0.45 and 20x/0.75 objectives. The dyes stained older bone matrix in light pink, whereas younger bone stained dark pink. Cell nuclei, fibrous and adipose tissue were stained blue. Descriptive histological evaluation was performed on a selected region of interest in the cortical and bone marrow cavity at the bone-implant interface.

2.5. Statistical analysis

Prism software (GraphPad Prism version 8.2.1.) was used for the statistical analysis. Statistically significant differences and comparisons of nonparametric independent samples were performed using Kruskal-Wallis tests with Dunn's multiple comparisons post hoc tests. Statistical significance was considered when $p \leq 0.05$.

3. Results

3.1. Characterization and microstructure description of the as-received screw

To characterize the ZX00 screw surface in terms of its topographical and physicochemical properties, SEM and CLSM were used to visualize and quantitatively analyze the surface topography on three regions of interest (the head, the valley, and the tip, Fig. 1a). SEM images in Fig. 1b–d depicted the cutting tool-induced periodic hierarchical patterns perpendicular to the long implant axis dominated the surface topography. The initial surface roughness was uniform on the entire screw with an average surface roughness (R_a) of 0.3 μm in the head and the tip, and R_a of 0.4 μm in the valley, which according to Albrektson and Wennerberg [84] classifies the ZX00 screw investigated in this work as an implant with smooth surface roughness. EDX measurements at the different parts of the screw (Table S1) revealed the presence of Mg, Zn, Ca and a trace amount of O suggesting the formation of a thin oxide layer on the surface of the screw due to contact with air and moisture occurring during manufacturing or cleaning procedures.

Backscattered electron (BSE) SEM images revealed nonuniformly distributed course intermetallic particles (IMPs) enriched in Ca (marked by the red arrows in Fig. 2a–c) in the ZX00 alloy. The Zn/Ca atomic ratio of the representative EDX point analyses performed on IMPs was much less than 1.23 suggesting that the Mg_2Ca forms in the alloy [39,85]. The presence of Mg_2Ca is also confirmed by XRD (Fig. 2m). IPF maps of the cross-sections that are perpendicular to the extrusion direction clearly indicated that the microstructure of the different screw zones varied in terms of grain size and crystallographic orientation (Fig. 2d–f). The average grain size calculated based on the equivalent dimension (d_{avg}) is the highest for the head zone (2.15 ± 0.10 μm), while the average grain sizes in the valley and tip regions are found to be 1.90 μm ± 0.06 μm and 1.91 μm ± 0.07 μm, respectively. Nevertheless, it must be underlined that the microstructure of the screw head is composed of elongated grains which are surrounded by very fine grains (Fig. 2d). This is a typical microstructure with non-recrystallized areas (the elongated primary grains) and the small grains which were refined continuously by the dynamic recrystallization (DRX) [86–88]. It is clearly shown that the recrystallization processes in the valley and the tip of the screw were more intense which is, in our opinion, most likely related to the turning procedure. The microstructure of the valley and the tip of the screw is composed of randomly distributed greater grains surrounded by very fine equiaxed grains (Fig. 2e and f). Grains formed in the head of the screw also have a random crystallographic orientation with the prevalence of the grains oriented to {2-1-10} (blue color) (Fig. 2e and f). Importantly, the average grain size for each screw zone is different. The largest average grain size was observed in the screw head. Due to the different recrystallization stages, the screw valley and tip displayed decreased grain sizes. The Kernel average misorientation (KAM) maps imply a strong heterogeneous distribution of dislocations in the elongated grains observed in the head zone of the screw. The accumulation of dislocations in both the valley and tip regions was also observed. They were accumulated along the grain boundaries and their higher intensity is observed in the tip of the screw (Fig. 2j–l).

3.2. In vitro testing

3.2.1. Immersion tests

The CR of the entire screws was measured based on the immersion tests in α-MEM solution supplemented with 10% FBS and 1% P/S. The ZX00 screws were exposed for 3, 6, 14, 21, and 28 days. Fig. 3a displays the calculated CR based on mass loss measurements and μCT data. Both methods of CR calculation demonstrated the same tendency for the CR to increase as immersion time increased. A near-linear increase in CR is

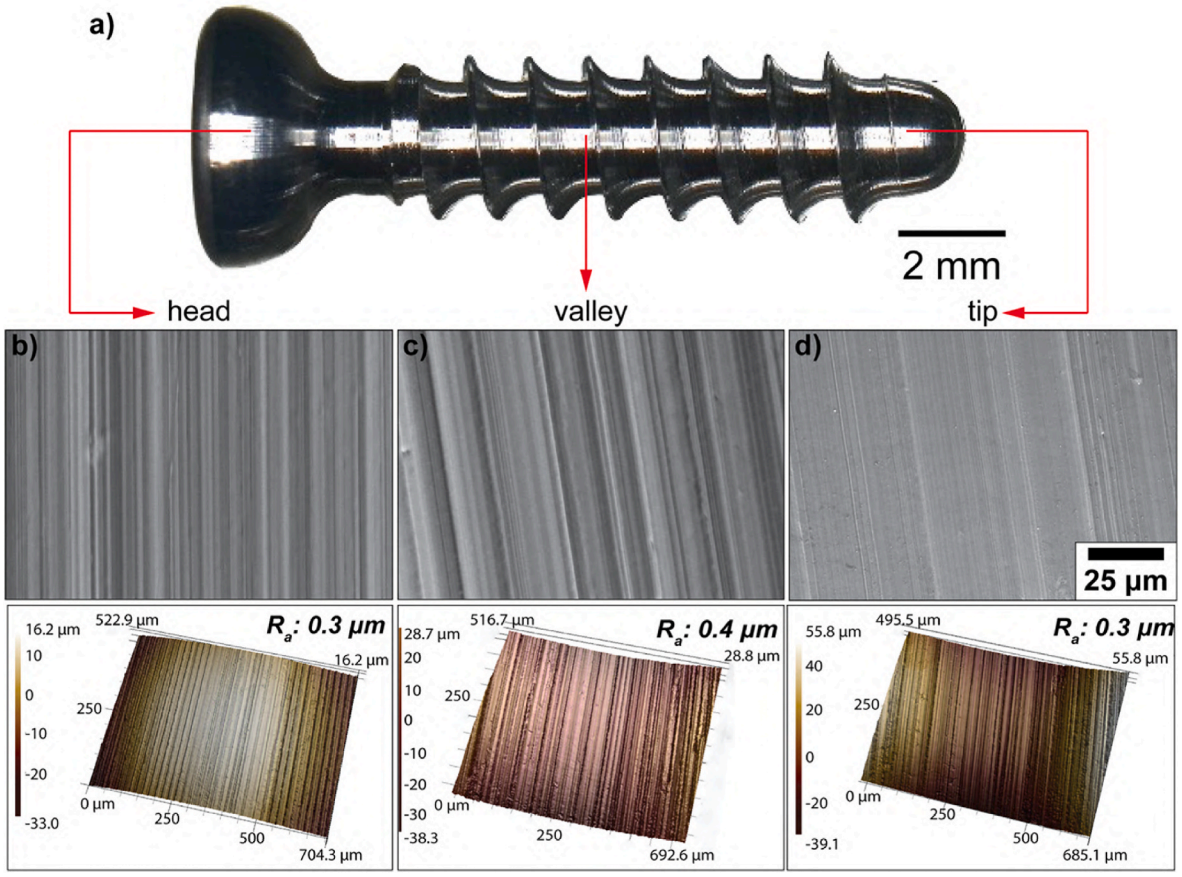

Fig. 1. Surface characterization of the ZX00 screw. a) Stereomicrograph of the overall screw. Representative SEM images of **b)** the head, **c)** the valley and **d)** the tip zones with the corresponding surface roughness before *in vitro* and *in vivo* testing. (The figure should be printed in color).

observed as immersion time increases (Fig. 3b). The largest variability between CR measurements calculated based on the mass loss measurements is observed at the beginning of immersion. After 3 days of testing the CR was found to be 0.74 mm × year^{-1}. The pH of the solution increased abruptly during this short time of immersion, indicated by the color change of the immersion solution from light to intense pink (Fig. S3). After 3 days, the pH did not change markedly and stabilized after longer immersion times (Fig. 3c). The evident increase in the pH of the solution with the immersed screws is a result of the screw's degradation and the formation of hydroxide ions during the initial degradation of the ZX00 screw.

After 6 days of immersion, the CR increased to 1.18 mm × year^{-1}. Afterwards, the CR slightly decreased to 0.93 and 0.97 mm × year^{-1} after 14 and 21 days of immersion, respectively. During the remainder of the experiment, the corrosion processes slowed down, and the calculated CR was found to be 1.04 mm × year^{-1}. Based on the validity of the linear regression of the CR plot, one can assume that the corrosion rate increases after 25 days of the immersion when the real values of CR increase are located above the red line (Fig. 3b). The increased osmolality of the immersed samples compared with the control α-MEM solution indicates that the cell culture conditions accelerated the degradation rate of the analyzed material (Fig. 3d) [89,90].

To have a greater understanding of the degradation parameters of the screws, stereomicroscope, and SEM observations (from surface and cross-sections) were taken after 3-, 6-, 14-, 21-, and 28- days of immersion. As depicted in Fig. 4a, the as-received surface of the screw was smooth and sharp threads were well-defined. With the increasing immersion time, the surface of the screw starts to become rough, more irregular, and uneven. Further, the entire screw surface turned black and was covered with white corrosion products (Fig. S4), which appeared as cracked corrosion films under SEM (Fig. 4b–f). After 14 days of immersion, the corrosion products tended to peel off and the screws progressively lost their sharp contours due to the substantial dissolution of the threads, which was particularly noticeable after 28 days. After immersion, the corroded surfaces were mainly composed of O, Mg, P, Ca and a trace amount of Zn and Cl (Fig. 4). A slight increase in the concentration of O and Ca, homogeneous distribution of P and a decrease in Mg content was observed as the immersion time increased.

The thickness and the chemical composition of the corrosion layer were also assessed on the cross-sections using EDX line scans and elemental distribution maps for O, Mg, P, and Ca (Fig. 5a–e), and EDX point analysis (Fig. S5). C was not considered for the semiquantitative analysis since cross-sections were sputtered with it and because of the C contamination built up during SEM energy-dispersive X-ray spectroscopy (EDX) [91]. The EDX elemental mapping and line scan analysis revealed that the corrosion layers consisted primarily of O, Mg, P, and Ca with traces of Zn. O and Mg concentrations were consistently higher than P and Ca concentrations at all immersion times. The ratio of Mg/O and Ca/P ratios were approximately 0.5 and 1.40, respectively. As observed in Fig. 5f, the corrosion layer thickness increased from 6.2 ± 6.1 μm after 3 days of immersion to 56.8 ± 29.3 μm after 28 days.

For further comparison with EDX analysis, Fig. S6 depicted the total prediction fraction diagram of Mg chemical compounds as a function of pH. According to the fraction equilibrium diagrams, in α-MEM solution supplemented with 10% FBS and 1% P/S, the corrosion products may be composed of $Mg(OH)_2$, $MgHCO^{3+}$, $MgHPO_4$, $CaMg(CO_3)_2$, and $MgCO_3$, while $MgSO_4$ is one of the inorganic salts in the medium composition. Between the pH range throughout the immersion test, higher calcium magnesium carbonate compounds formed up to 14 days of immersion and then began to decrease, while magnesium carbonate compounds

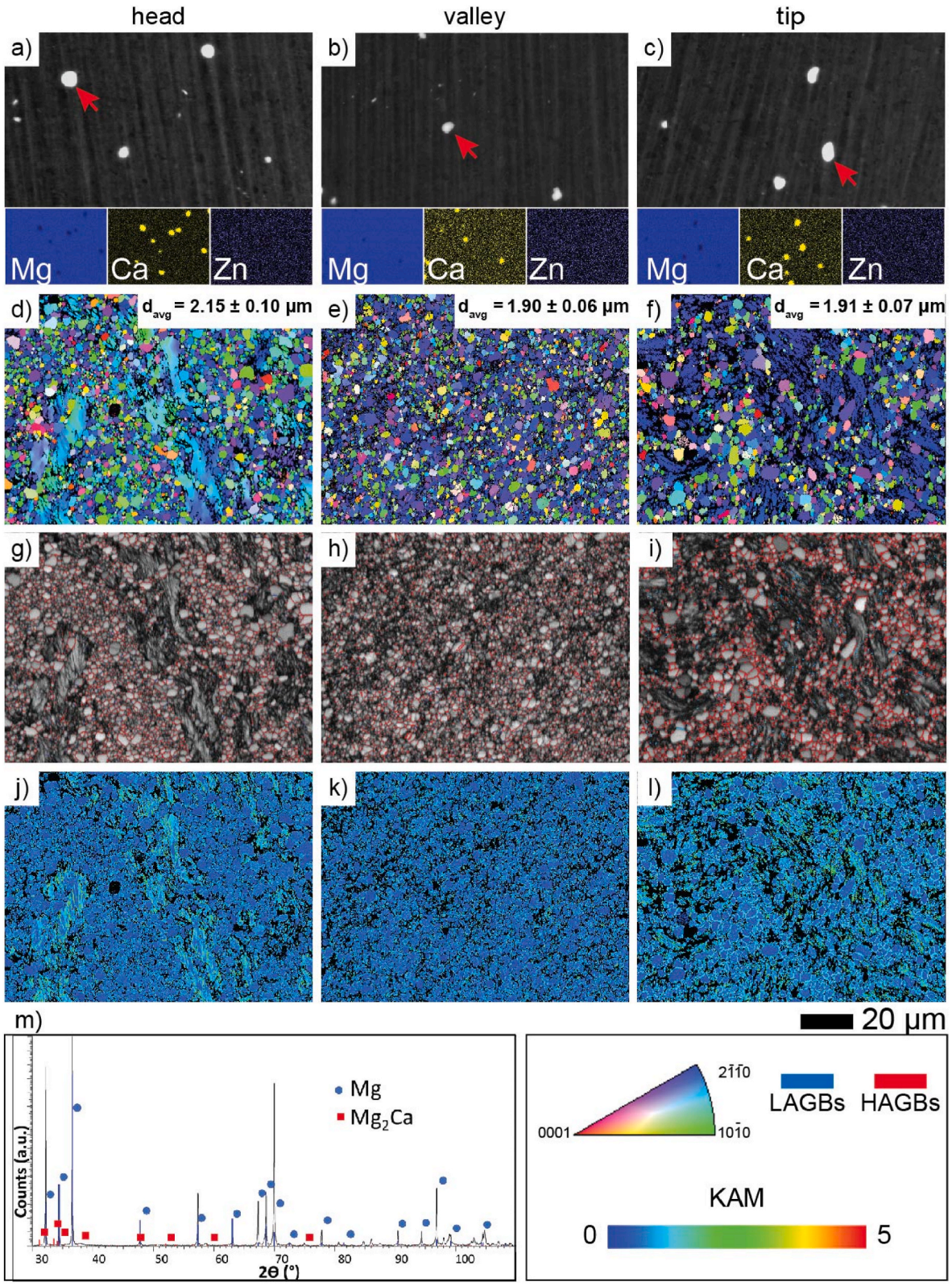

Fig. 2. Microstructural characterization of various regions of ZX00 screws before *in vitro* immersion and *in vivo* implantation. SEM images with the corresponding EDX maps and the equivalent dimensions for grains (**a–c**), inverse pole figure (IPF) maps with the average grain size (**d–f**), grain boundary (GB) distributions (**g–i**), Kernel average misorientation (KAM) maps (**j–l**), and X-ray diffraction patterns of the ZX00 alloy (**m**). (The figure should be printed in color).

increased in the experimental pH range.

High-resolution XPS spectra for the head and the valley after 3 days of *in vitro* immersion shown in Fig. 6 also agree with EDX analysis. The O 1s peak was deconvoluted and fitted with OH^- at 532.7 eV, O^{2-} at 530.9 eV, and H_2O at 534.4 eV, O–Mg at 528.9 eV (Fig. 6a). The Mg 1s peak was used to identify Mg compounds, as it is depicted in Fig. 6b. The spectrum from 1299 eV to 1318 eV was deconvoluted and fitted with Mg $(OH)_2$ at 1303.0 eV, $MgCO_3$ at1305.3 eV and $Mg(CO_3)_4(OH)_2$ at 1306.8

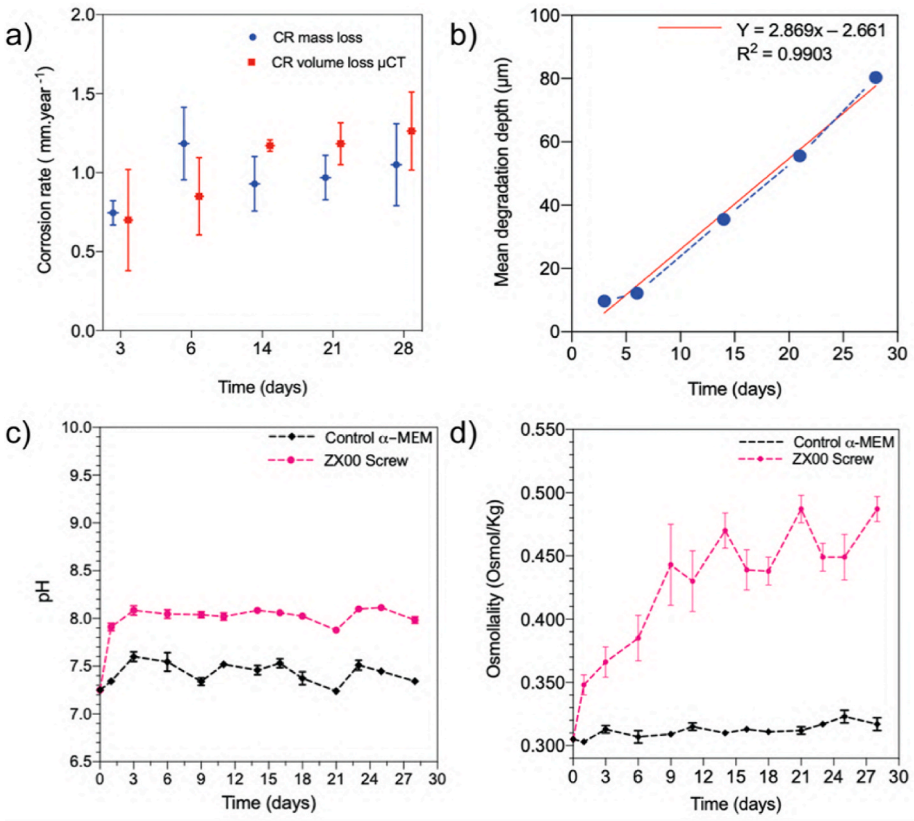

Fig. 3. Degradation parameters for ZX00 screws during immersion in *α*-MEM culture medium supplemented with 10% FBS and 1% P/S under cell culture conditions: a) CR calculated based on mass loss (denoted in blue) and volume loss obtained from µCT measurements (denoted in red), **b)** mean degradation depth as a function of the immersion time with the linear approximation of the measured data, **c)** pH and **d)** osmolality measurements during 28 days of immersion. (a) and (b) (n = 3/time point); (c) and (d) (n = 6/time point). Data presented as mean ± standard deviation. (The figure should be printed in color).

eV [92–95]. The signals obtained in the valley and the tip were fitted with the same peaks, therefore, high-resolution spectra for one of them are shown (for the valley, Fig. 6 c-d). The shape of the peaks of the head and the valley are different since the number of components in the corrosion products varied. The corrosion products formed on the valley and tip were composed of Mg 1s, O 1s, Ca 2p and P 1s [96]. We observed also Ca 2p high-resolution spectra with the binding energy best fit CaMg $(CO_3)_2$.

To analyze the surface and corrosion layer formed after the specific immersion times, µCT images of the screws were reconstructed before and after the removal of the corrosion layers. Fig. 7 depicts the reconstructed µCT images and calculated surface area values of the screws after immersion (A_i) and after the removal of the corrosion layer (A_d). The µCT reconstruction of the as-received screw and after 3 days of immersion is shown in Fig. 7a. Due to the limitations of µCT resolution, it was not possible to distinguish the degradation layer after 3 days of immersion. After 6 days of immersion, only a few pits are observed on the screw after corrosion product removal (Fig. 7b). More intense corrosion damage was visible after 14 and 21 days of immersion (Fig. 7c and d, respectively), and the well-developed surface of the screw resulting from the intense corrosion processes could be observed. The greatest difference between A_i and A_d was found after 28 days of immersion (Fig. 7**e**).

The significant difference between A_i and A_d indicates that, due to the intense corrosion processes, thick corrosion products were formed as the immersion time increased, confirming the corrosion thicknesses measurements performed on BSE images (Fig. 5f). However, these corrosion products were porous and therefore cannot protect the surface of the screw.

3.2.2. *Electrochemical response of various regions of the screw*

The CR calculations are the most appropriate method for analyzing the overall corrosion propagation of various materials. However, in this work, we would like to focus on the variables in the kinetics of the corrosion processes on the different zones of the screw, which is extremely important from the biomedical point of view. The electrochemical measurements were performed in a PBS solution. Fig. 8a shows the evolution of the corrosion potential (E_{corr}) of the samples exposed to PBS solution under open circuit conditions for 1 h. The E_{corr} recorded for the head and tip of the screws did not change significantly during the experimental time. The lowest value of E_{corr} was recorded for the screw head (~-1.92 V/Ref). The tip of the screw had an E_{corr} value of ~ -1.90 V/Ref). The screw valley had the greatest E_{corr} value, with some fluctuations visible over the time of immersion which is characteristic of the valley. The E_{corr} of the screw valley was initially −1.85 V/Ref, decreased to ~ -1.87 V/Ref, and approached −1.80 V/Ref at the end of the immersion. The polarization curves obtained for the samples are given in Fig. 8b. For Mg-based alloys, the cathodic range of the curves represents the cathodic hydrogen evolution, and the anodic side of the curves represents the dissolution of Mg [97–99]. The shape of the recorded polarization curves was similar. However, the curves were recorded over various ranges of current density and potential. Noticeably, all the curves exhibited a breakdown potential (E_b), which for the head was found to be −1.70 V/Ref. For the screw valley and the tip, the E_b values were −1.65 V/Ref and −1.71 V/Ref, respectively (Table 1). The corrosion potential (E_{corr}) and corrosion current density (i_{corr}) were derived directly from the polarization curves, and they are listed in Table 1. The results show that the highest i_{corr} of 32 µA/cm^2 and the most positive E_{corr} of −1.82 V/Ref values were characteristic for the head of the screw. Also, the passivation region recorded for the screw head sample was the narrowest among all analyzed specimens. Such a small difference between E_b and E_{corr} indicates that passivation processes are limited. The E_{corr} and i_{corr} calculated for the valley and the tip zones were similar (E_{corr} of −1.86 V/Ref and E_{corr} of-1.85 V/Ref, and i_{corr} of 21 µA/cm^2 and i_{corr} of 24 µA/cm^2, for the valley and the tip, respectively). Generally, the highest i_{corr} values were exhibited by materials with the highest CR values [21,100,101].

However, in the case of Mg-based alloys, corrosion resistivity cannot

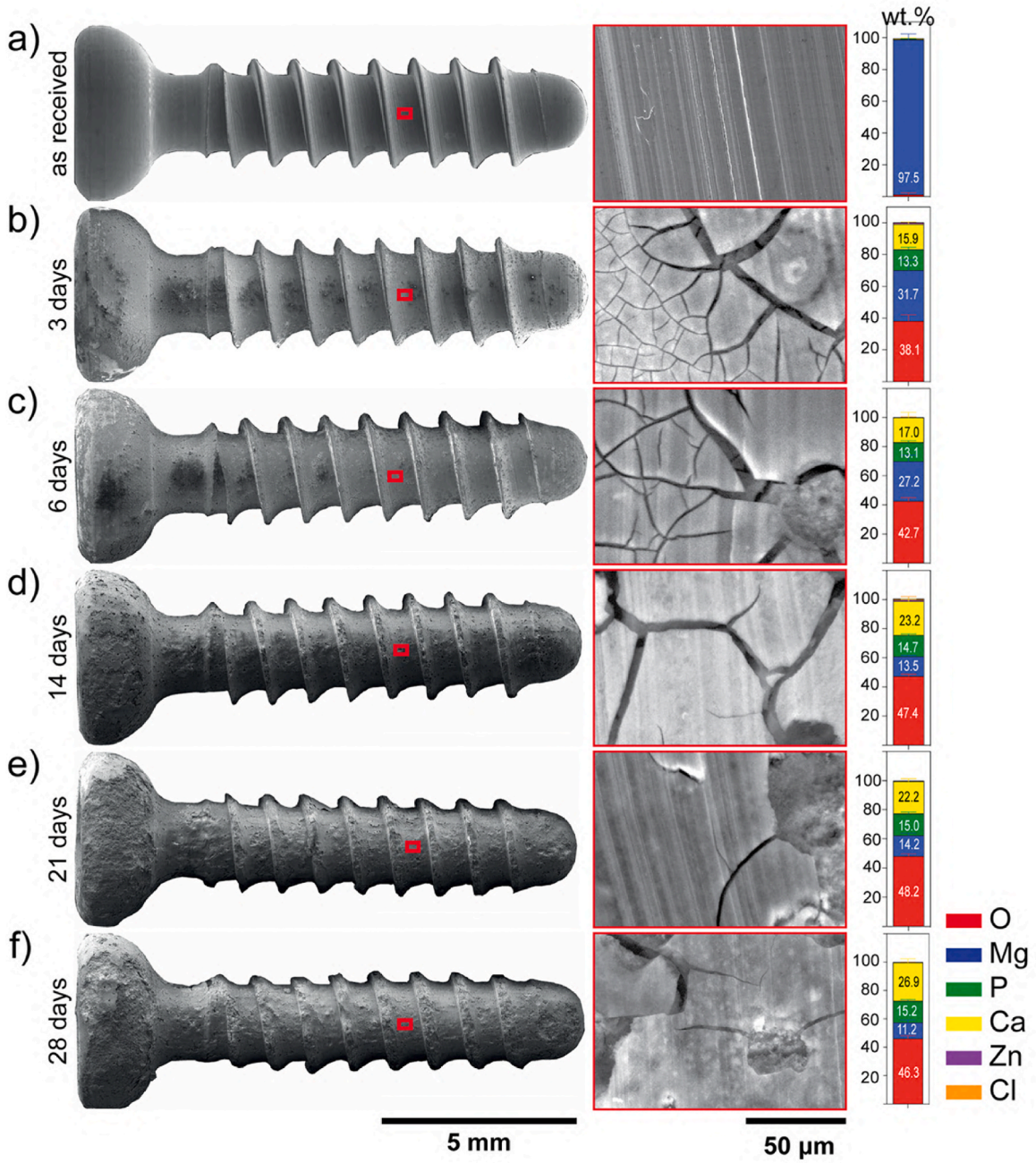

Fig. 4. Surface characterization of the corroded screws under cell culture conditions exposed to α-MEM culture medium supplemented with 10% FBS and 1% P/S. SEM images of the screw and a representative image of the surface and EDX analysis of the corrosion products performed after each period of immersion: **a)** before immersion, **b)** after 3-, **c)** 6-, **d)** 14-, **e)** 21-, and **f)** 28- days of immersion. EDX data presented as mean ± standard deviation (n = 54 EDX point measurements/time point from 3 independent samples/time point). (The figure should be printed in color).

be simply described based on the potentiodynamic results because of the negative difference effect [102]. To confirm the differences in the corrosion behavior of the various zones of the screw, EIS was performed (Fig. 8c and d). The obtained data were fitted with the equivalent electrical circuit (Fig. 8e). Two capacitive loops and one inductive loop in a low frequency can be recognized in the Nyquist plots recorded for all areas of the screw. The proposed circuit includes solution resistance (R_s), a constant phase element (CPE_{ct}), and a resistance (R_{ct}) which are associated with the double layer and charge transfer resistance. The diffusion of the ions through the porous corrosion layer is described by the R_{diff} and CPE_{diff}. The inductance (L) in series with the resistance (R_L) characterizes the inductive behavior at low frequencies (Table 2) [103, 104].

The data presented in the form of Nyquist plots and Body graphs (Fig. 8c and d) show that the order of the corrosion resistance for the various zones of the screw is: the valley > the tip > the head. This conclusion keeps highly consistent with the results of the potentiodynamic curves. Generally, the CR inversely scales with the polarization resistance ($\sim R_p^{-1}$). R_p, in turn, correlates with the impedance at zero frequency [102]:

$$\frac{1}{R_p} = \frac{1}{R_1 + R_2} + \frac{1}{R_3} \quad (5)$$

Based on the equivalent electronic circuit given in Fig. 2, the total calculation of R_p can be estimated by:

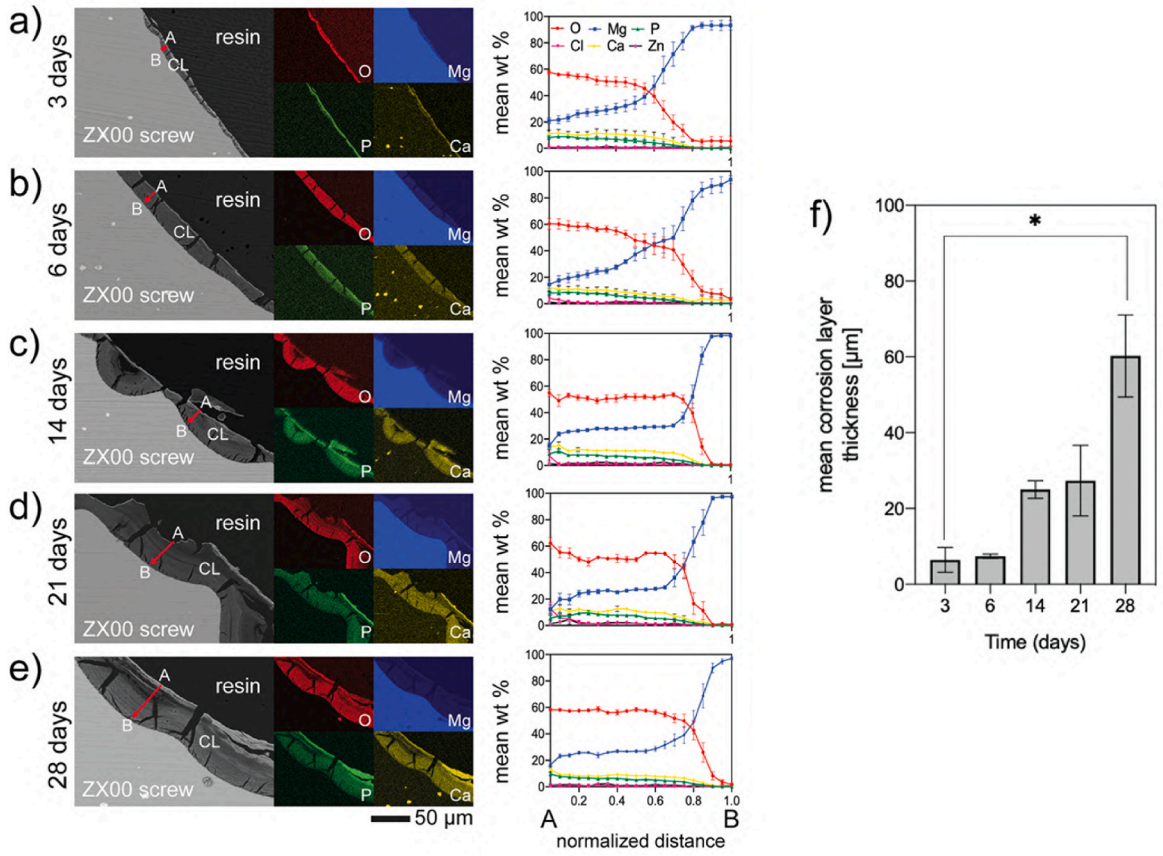

Fig. 5. Cross-sectional characterization of the corrosion layers after *in vitro* degradation. Representative SEM images of the corrosion layers (CL) and corresponding EDX mapping, and line scans following the direction marked by the red arrows (from the outer layer (A) to the inner layer (B) of the corrosion products formed on the ZX00 screw: **a)** after 3-, **b)** 6-, **c)** 14-, **d)** 21-, and **e)** 28- days of immersion. Data presented as mean ± standard error of the mean (SEM) (n = 7–9-line scans/time point from 3 independent samples). **f)** Changes in the corrosion layer thickness as a function of time. Data presented as mean ± standard deviation (n = 150–300 measurements/time point from 3 independent samples); *$p < 0.05$ versus day 3 and 28. The Kruskal-Wallis test was used for comparison between time points. (The figure should be printed in color).

$$\frac{1}{R_p} = \frac{1}{R_{ct} + R_{diff}} + \frac{1}{R_L} \tag{6}$$

Therefore, the apparent differences between the corrosion performance of various zones of the screw are confirmed by the values of R_p (Table 3). The most corrosion-resistant zone is the valley of the screw. The screw tip is less corrosion-resistant, and the head of the screw is the least resistive.

3.3. *In vivo testing*

The surface morphology of the retrieved ZX00 screws without the surrounding bone tissue after 6-, 12-, and 24- weeks of *in vivo* implantation were characterized by SEM/EDX (Fig. 9). The surface of the screw before implantation is uniformly smooth with sharp threads (Fig. 9a). After 6 weeks of implantation, the surface morphology of the screw became rough. The threads began to lose their sharp contours, and a cracked corrosion layer formed on the implant surface (Fig. 9b). With increasing implantation time (after 12 weeks), the threads and valleys beneath the head (shaft zone) became more corroded than those in the tip zone (Fig. 9c). After 24 weeks, the implants maintained their screw shape with an uneven, corroded, cracked surface. However, the threads were worn away (Fig. 9d). At 24 weeks of implantation, a tight bone-implant contact was observed below the head, in the shaft zone. This tight contact at this advanced state of bone integration did not allow bone tissue removal without damaging the corrosion layer and the screw implant. In addition, the cracks visible on the corrosion layer presumably resulted from the dehydration of the corrosion products during the sample preparation [105–111]. The EDX examination of the retrieved screws at the head, the shaft and the valley zones revealed a homogeneous distribution of P and Mg, a slightly higher concentration of O with the increasing implantation time, and a high Ca concentration in the shaft and head zone at 6 and 24 weeks, respectively (Fig. 9e). Some bone tissue remained attached to the surface of the implant as observed in Fig. S7. The tip zone of the screws was sometimes in contact with cortical bone and other times were within the intramedullary cavity in different samples at the different time points in the different retrieved screws analyzed. As a result, the chemical composition of the corrosion products formed in this screw region was performed on cross-sections of the bone-implant resin-embedded specimens.

To further understand the degradation of the ZX00 screws, the corrosion layers at the bone-implant interface were analyzed in detail. As shown in Fig. 10, the thickness, distribution, and extent of the corrosion layers formed on the screws during implantation as well as their chemical compositions was implantation-site-dependent. Therefore, two distinct screw zones were characterized: those in contact with cortical bone and those within the intramedullary cavity. In regions where the implanted screw was in early direct contact with the cortical bone, a non-uniform corrosion layer formed at 6 weeks with a mean thickness of 19.8 ± 17.3 µm. A two-fold and three-fold increase in the thickness of the corrosion layer formed in the cortical bone compartment were observed after 12- and 24- weeks, respectively (39.8 ± 27.4 µm after 12- weeks, and 61.9 ± 34 µm after 24 weeks of implant placement) (Fig. 10a, c). The formation of thick corrosion layers in the

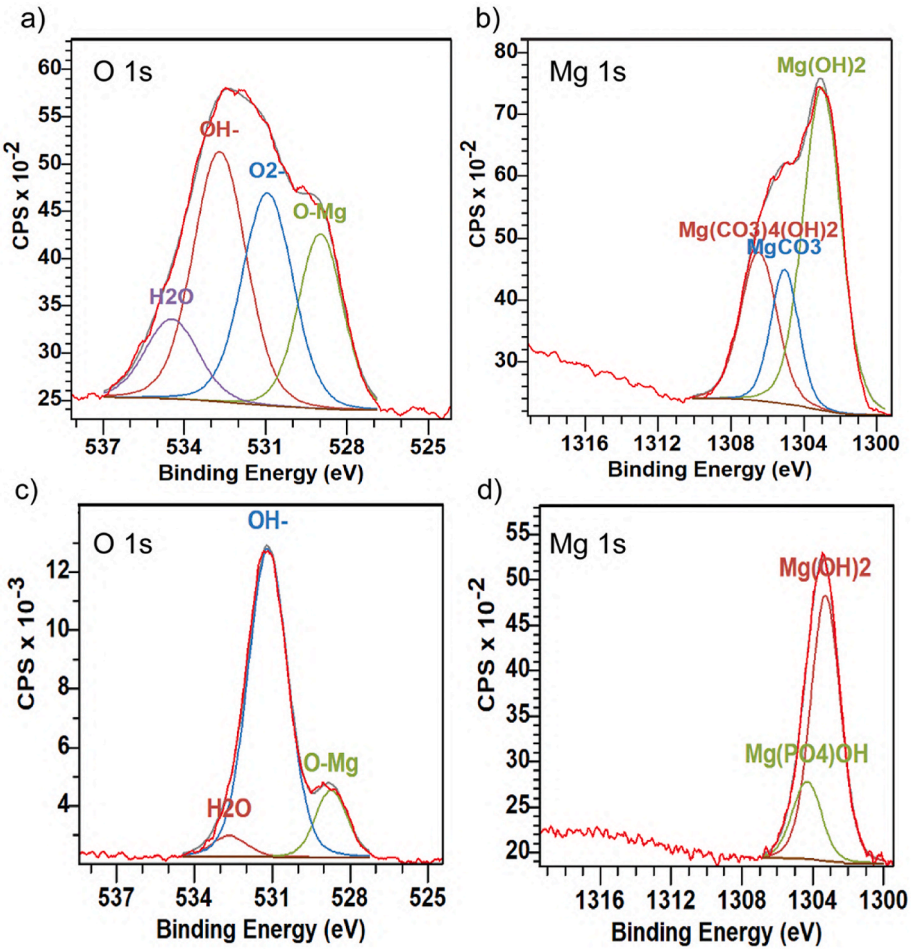

Fig. 6. High-resolution XPS spectra on various regions of a ZX00 screw performed after 3 days of *in vitro* immersion in α-MEM solution supplemented with 10% FBS and 1% P/S. a) and b) O 1s and Mg 1s spectra for the head, respectively. c) and d) O 1s and Mg 1s spectra for the valley. (The figure should be printed in color).

intramedullary cavity was observed at all-time points, with a mean ranging from 51.9 to 65.3 μm (Fig. 10b and c). However, the larger standard deviation shown in Fig. 10c was a result of the irregular thicknesses of the corrosion layer observed in the intramedullary cavity from sample to sample, with zones reaching thicknesses up to ~174 μm. Interestingly, after 6 weeks of implantation, the corrosion products in the intramedullary cavity were not in contact with bone, whereas bone contact was found in a few zones at 12 weeks and in the close vicinity of the corrosion products within the intramedullary cavity after 24 weeks (Fig. 10b). Similar to what was observed in the cortical bone, the corrosion layer that formed in the head zone increased in thickness from 18.2 μm after 6 weeks to 63.2 μm after 24 weeks (Fig. S8a). Corrosion layers with non-uniform thickness were also observed in the tip zone because this region of the screw was sometimes in contact with cortical bone and sometimes within the intramedullary cavity (Fig. S8b).

Fig. 10 also summarizes the results of the elemental mapping and line scan investigations as well as BIC data obtained by BSE images of the dissected diaphysis of the sheep tibia cross sections. At all implantation times, the corrosion products were composed of O, Mg, P, Ca, and traces of Zn. The detected amount of Zn was negligible for all samples. Therefore, the corresponding mapping is not depicted. Ca and P elemental maps reveal the deposition of Ca and P in the newly formed bone in the peri-implant region. The line scans performed from the outer part of the corrosion layer to the residual implant revealed compositional changes within the degradation layers. After 6 weeks of implantation, O and Mg were homogeneously distributed within the corrosion layers while higher concentrations of Ca and P were detected in the outer part of the corrosion layers in the intramedullary cavity. After 12 and 24 weeks, Mg, O, P, and Ca were steadily distributed within the corrosion layer, with slightly higher Ca and P content detected at the outer part of the corrosion products in the head zone after 24 weeks (Fig. S8a). Interestingly, after 6 and 12 weeks of implantation, only trace amounts of Ca, P, and Zn were observed in the thin degradation layer formed in the areas in contact with the cortical bone (Line scans in Fig. 10a). O and Mg were present at higher concentrations, indicating that Mg hydroxide $Mg(OH)_2$ was the main corrosion product formed in this bone compartment. Similarly, lower amounts of Ca and P were uniformly distributed in the corrosion layer formed in the intramedullary cavity after 24 weeks (Fig. 10b). In addition, EDX point analyses were conducted in randomly selected cortical bone zones adjacent to the corrosion layer at each time point. O concentration was high at all implantation times, P and Ca content were steadily distributed, and traces of Mg were found at all time points. The Ca/P ratios of bone in the vicinity of the corrosion layer were 1.63 ± 0.02, 1.63 ± 0.13, and 1.50 ± 0.04, after 6, 12, and 24 weeks after implant placement, respectively, with no statistically significant differences between time points (Fig. 10d). With the extension of implantation time, an increase in BIC %, in the cortical bone and the intramedullary cavity was observed without significant differences between all three different implantation periods (Fig. 10e). The BIC for the cortical bone zone were measured at the shaft and the first thread below the head while the BIC measurements for the intramedullary cavity were performed at the middle section of the screw since this section was always located within the intramedullary cavity in all explants. (As illustrated in Fig. 12(a–c),

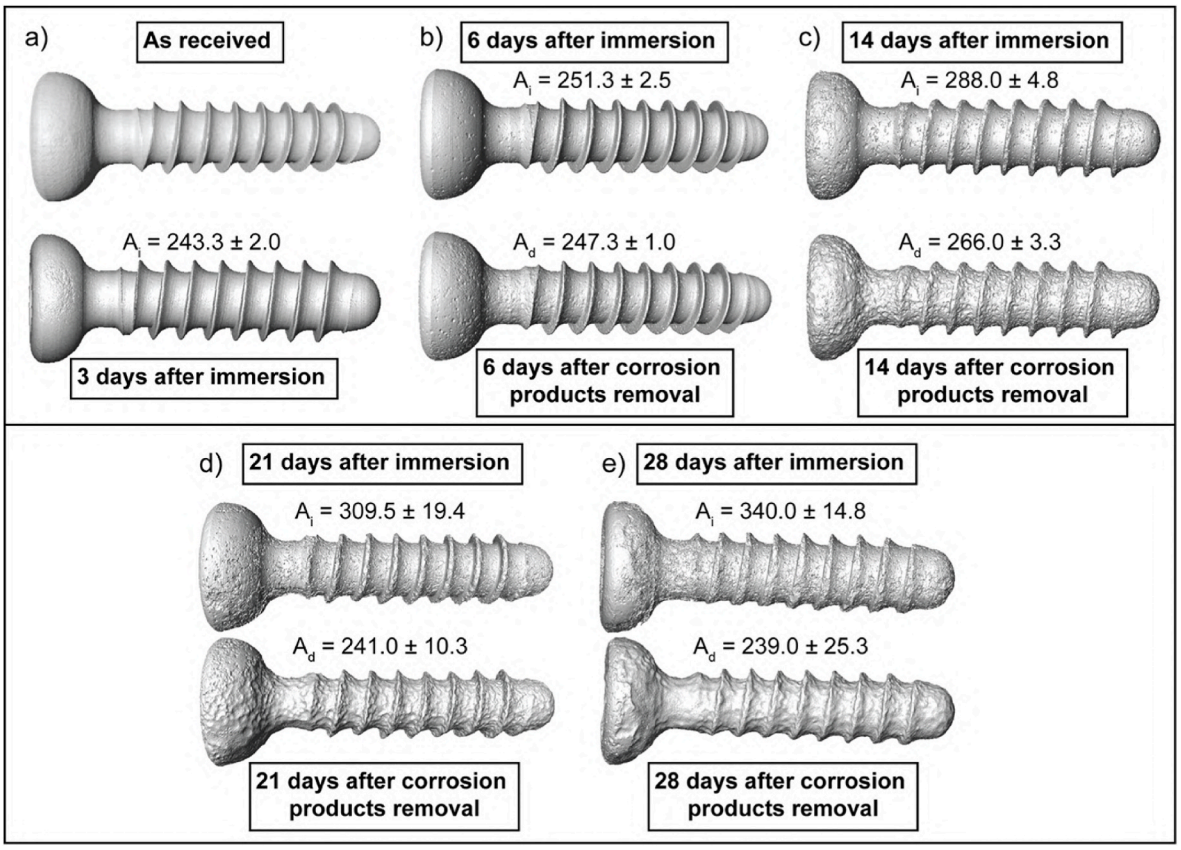

Fig. 7. Characterization of the corroded ZX00 screws reconstructed based on the μCT data μCT reconstructed images are displayed after immersion in ***α***-MEM culture medium supplemented with 10% FBS and 1% P/S under cell culture conditions and with subtracted corrosion layers: **a)** as received screw and after 3 days of immersion, **b)** after 6-, **c)** 14-, **d)** 21-, and **e)** 28 -days of immersion with the corresponding surface area after immersion (A_i) and after corrosion layer removal (A_d). Data presented as mean ± standard deviation (n = 3/time point).

yellow and green dotted rectangles for cortical and intramedullary cavity regions, respectively).

Fig. 11 depicts μCT reconstructions (2D and 3D) of the degradation performance for the implanted ZX00 screws, in which continuous and uniform degradation of the ZX00 is observed. After 24 weeks, the implanted screws were well preserved. Different regions of the implant were exposed to distinct bone compartments. Some screw threads below the head and some tip regions of the inserted screws were embedded in the cortical bone, while the middle section was exposed to the bone marrow cavity. After 6 weeks, the μCT scan images showed that significant gas was released around the implant and gas voids were primarily identified within the medullary cavity (Fig. 11, red asterisks). After 12 weeks, the gas voids were still detectable, while at 24 weeks, they were barely apparent on μCT. In addition, the threads maintained their sharp shape until 12 weeks post-surgery. After 24 weeks of implantation, reduced and smoothed thread crests were observed, consistent with our *in vitro* findings.

Histological analysis was performed on selected zones in the cortical bone and the intramedullary cavity compartments to obtain information about the bone tissue response. At all-time points, cortico-periosteal reactions, appositional growth, and new bone formation in the endosteum zone were observed (Fig. 12 a–c, red arrows). In regions where the implanted screw made early contact with the cortical bone, a thin layer of corrosion products was observed (Fig. 12d, black arrows) while in the medullary cavity, thicker corrosion products were seen (Fig. 12e, black arrows). In some cases, osteoblasts (Ob) were connected to the newly formed bone (Fig. 12d, small inset square). Gas voids (gb) were surrounded by thin fibrous tissue in the cortical and intramedullary cavity compartments (Fig. 12d and e). New bone (nb) formation was observed in the cortical bone adjacent to the medullary cavity and around the gas voids. A cement line (*Cm* Ln) can be seen between new and pre-existing bone (Fig. 12e). In the cortical bone, after 12 weeks of implantation, along with the degradation, new woven bone formed in direct contact with the corrosion layer (Fig. 12f, yellow arrows). The irregular Haversian tissue and additional *Cm* Lns were also observed. Moreover, some newly formed osteoid tissue was observed in the cortical bone that surrounded the medullary cavity. (Fig. 12g, orange arrows). After 24 weeks, small gas voids remained surrounded by thin fibrous tissue in the cortical bone and medullary cavity compartments (Fig. 12h and i). Tight direct bone contact with the degradation products and the formation of new bone next to the ZX00 screws was observed (Fig. 12h and i, yellow arrows) which connected with the old, mature bone tissue. In the medullary cavity, new mineralized tissue in the form of parallel-fibered bone bridging the medullary cavity with thicker bone bridges formed on the corrosion products. Interestingly, the corrosion products formed on the 24 weeks inserted implants-stained pink, similar to the dark pink color of the newly formed mineralized tissue (Fig. 12h and i).

4. Discussion

The purpose of the present study was to evaluate the corrosion performance of ZX00 screws under *in vitro* and *in vivo* physiological conditions. As the interaction between the implant surface and the surrounding tissues is crucial to the success of a medical implant, influencing its corrosion behavior [112] and the biological response [113], the surface of the ZX00 screw was characterized in terms of surface roughness and its chemical composition before implantation. Our results revealed that the initial surface of the ZX00 screws was smooth, anisotropic and free of contaminants, with a thin oxide layer resulting from contact with air and moisture during the manufacturing

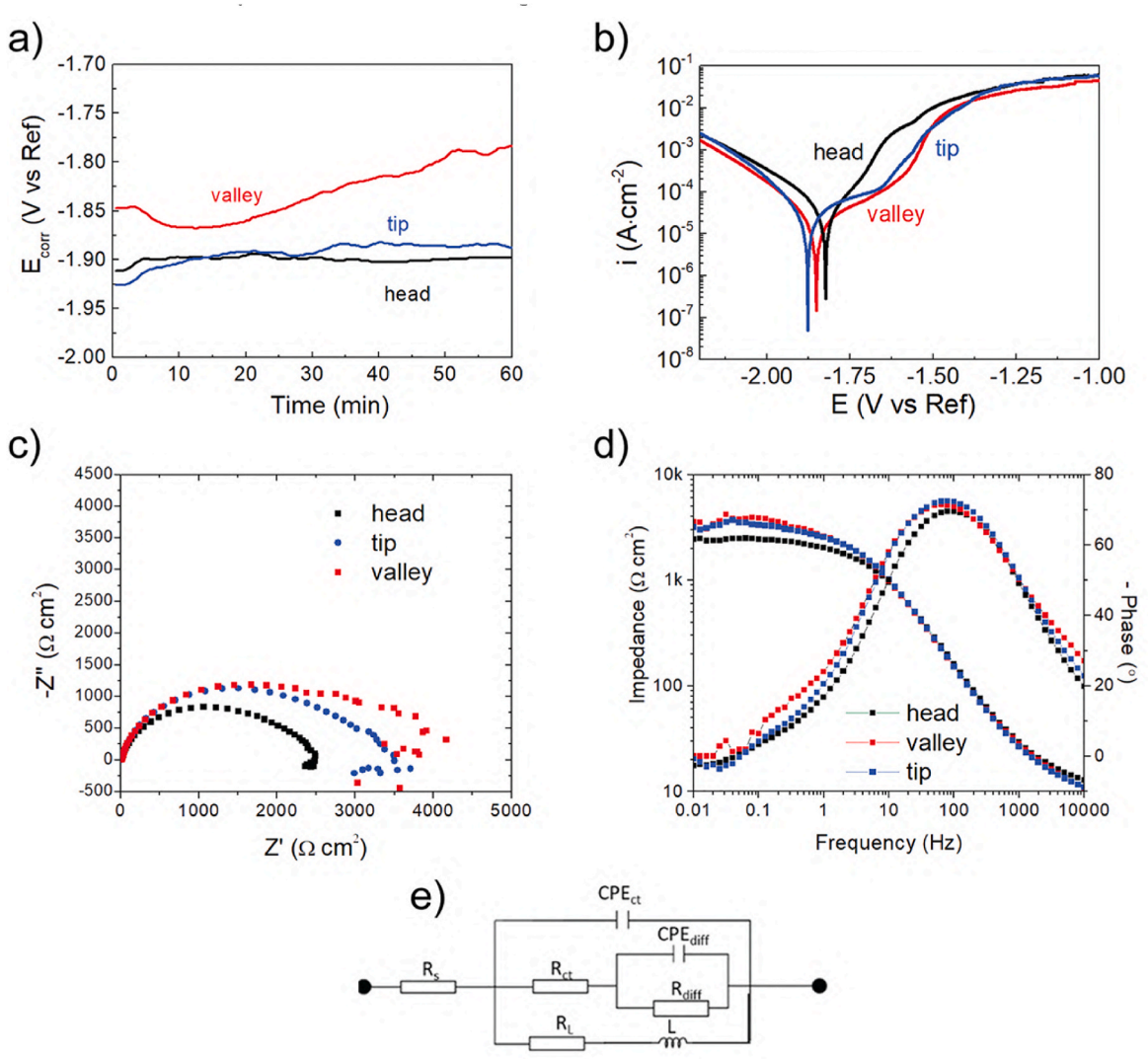

Fig. 8. Electrochemical corrosion data obtained for the various zones of the ZX00 screw after 1 h of immersion in PBS solution: a) E_{corr} evaluation, b) potentiodynamic curves, c) EIS Nyquist plots, d) EIS Body plots. (The figure should be printed in color).

Table 1
The electrochemical parameters of various zones of the ZX00 screw were extrapolated using the Tafel method.

Zone of the screw	E_{corr} (V/Ref)	i_{corr} (μA/cm^2)	E_b (V/Ref)
head	−1.82	32	−1.70
valley	−1.86	21	−1.65
tip	−1.85	24	−1.71

and cleaning process. In addition, no surface degradation was observed concerning packing and storage, as evidenced by the absence of O-enriched regions and adequate *in vivo* biocompatibility and degradation behavior. From the medical point of view, implants must withstand the standards of the cleaning and sterilization procedures without impairment of implant quality and safety. Specifically, the implants must be free of impurities that could embed into the surface of the screws during the different manufacturing stages, handling or packaging procedures prior to the surgical implantation [114–116]. It is essential to ensure that the surface properties of the implant remain unchanged during the storage [117] for the therapeutic use of Mg as biodegradable implants.

As proved based on EBSD data, the average grain size (d_{avg}) in the various regions of the screw changes: d_{avg} for the head was found to be the highest, while for the valley and the tip, it was lower and comparable to each other. Those results clearly confirm that the recrystallization and recovery processes in the case of the head, the tip and the valley, are various due to a long time of being in contact with the diamond tool during CNC processing. It is worth underlining that screws were manufactured using polycrystalline diamond tools without lubrication to avoid potential contamination and corrosive attack [39]. During

Table 2
Characteristic values were deduced from the measured impedance spectra by means of fitting the equivalent electrical circuit (EEC) shown in Fig. 3.

Zone	R_s (Ω cm^2)	R_{diff} (Ω cm^2)	CPE_{diff} (S·s^{a}cm^{-2})	a_1	R_{ct} (Ω cm^2)	CPE_{dl} (μS·s^{a}cm^{-2})	n_2	L (kH•cm^2)	R_L (Ω cm^2)
head	12	501	$1.6{\cdot}10^{-3}$	0.82	2196	26	0.84	67	19,000
valley	10	1154	$0.8{\cdot}10^{-6}$	0.99	3189	30	0.83	63	18,000
Tip	10	1040	$1.3{\cdot}10^{-3}$	0.81	2928	25	0.85	81	12,000

Table 3
Polarization resistance is calculated according to equation (6) from the values given in Table 2.

Zone of the screw	R_p (Ω cm^2)
head	2361
valley	3498
tip	2981

turning, uncontrolled heat is generated as a result of friction. For Mg alloys even such a slight local increase in temperature may cause microstructure reformation.

As per the results of this work, the *in vitro* corrosion rates of the ZX00 screw were lower than those calculated by Cihova et al. [40] for the implants made from ZX10 and ZX20, by Hofstetter et al. [24] for the implants made from ZX50 and Ibrahim et al. [118] who immersed Mg-1.2Zn-0.5Ca alloy in simulated body fluids (SBF). This is due to the different experimental parameters and immersion solutions employed, as well as related to the alloying elements in the matrix of the material, where the Zn concentration is lower in ZX00 than the previously mentioned alloys. This is mostly related to alloying elements in the matrix of the material, where the Zn concentration is lower in ZX00 than in ZX10 or ZX20. As the number of intermetallic phases containing Zn increases along with its concentration, a greater number of micro galvanic cells are formed. Our results also showed that there was a linear dependence on the corrosion rate even after 24 days of immersion. Similar results were shown by Zeller-Plumhoff et al. [119] where a computational model for pure Mg was utilized. However, our *in vitro* results revealed a higher corrosion rate than reported by Okutan et al. [44], who found a degradation rate of 0.29 ± 0.03 mm × year^{-1} of ZX00 pins after three weeks of immersion in simulated body fluids (SBF). As stated by Gonzalez et al. [89], the differences may be due to the use of different immersion solutions, which results in the formation of different degradation products. Furthermore, when implanted into the distal metaphysis and epiphysis of three-month-old lambs, ZX00 alloy corroded at a rate between 0.2 and 0.75 mm × year^{-1} [45], which is lower than our *in vitro* results where ZX00 screw corroded at a rate of 1.04 mm × year^{-1}. Consequently, identifying local *in vivo* environment parameters is essential for optimizing *in vitro* setups, leading to more accurate correlations between *in vitro* and *in vivo* data.

It is widely described in several publications that the kinetics of the corrosion process of Mg-based alloys in an aqueous environment is determined by the anodic and the cathodic reactions, resulting in a magnesium hydroxide $Mg(OH)_2$ formation, hydrogen gas release and local pH changes [89]. In a complex environment such as the human body, Cl^- ions make the protective layer soluble, and the presence of organic molecules can also influence the corrosion behavior [120] and the composition of corrosion products of the Mg-based devices. From our *in vitro* results, the ZX00 screw corroded nonuniformly with a corrosion layer forming on the surface of the screws composed of O, Mg, P, and Ca. As evidenced by the fluctuating *in vitro* osmolality, this corrosion layer did not cover the entire surface of the screws and did not compensate for the dissolution reactions. When released into the solution, soluble degradation products such as Mg^{2+}, Zn^{2+}, Ca^{2+}, and OH^- ions alter the pH and composition of the solution [121]. At the beginning of our immersion test (up to the 3rd day), a significant increase in pH of

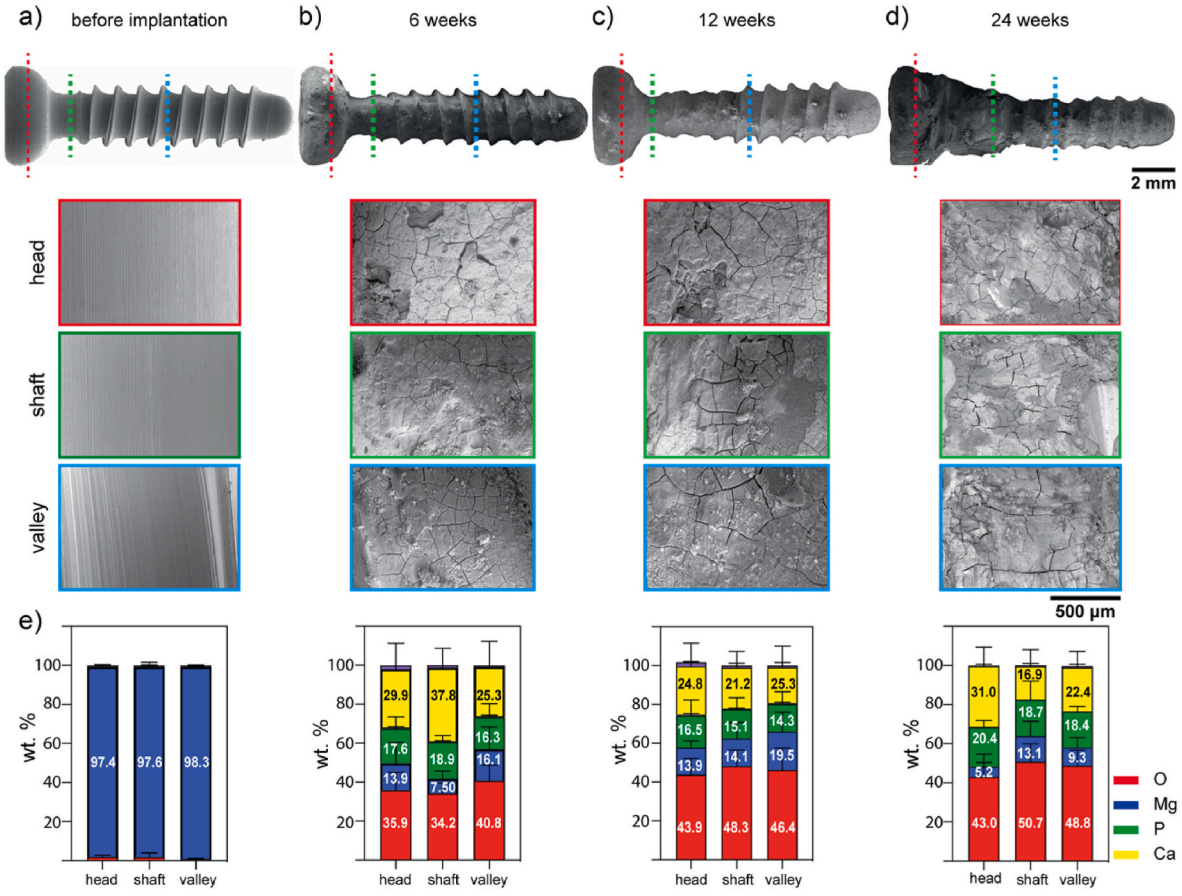

Fig. 9. Surface characterization of retrieved ZX00 implants after 6-, 12-, and 24- weeks of in vivo implantation. a) before implantation, **b)** after 6-, **c)** 12-weeks, and **d)** 24- weeks of implantation, **e)** corresponding EDX analyses of the corrosion products formed on the different screw zones: head – red dotted line, shaft –green dotted line, valley – blue dotted line. Data presented as mean ± standard deviation (n = 47–50 EDX point measurements/time point from 3 independent samples). (The figure should be printed in color).

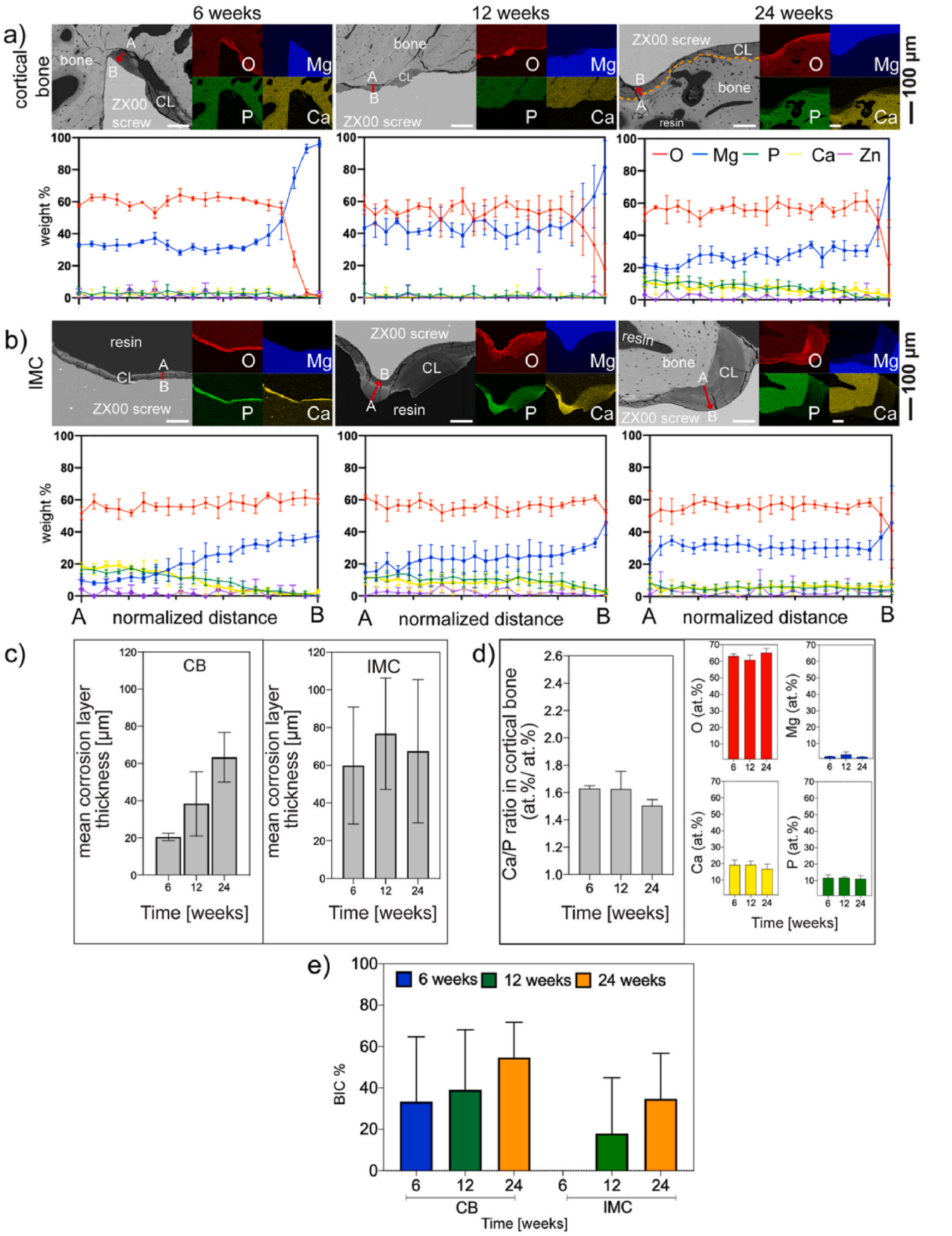

(caption on next page)

Fig. 10. Characterization of the bone-implant interface. SEM images of the ZX00-implant interface with its corresponding elemental distribution maps and line scans of the corrosion layers after 6-, 12-, and 24- weeks of *in vivo* implantation performed at **a)** cortical bone (CB), and **b)** intramedullary cavity (IMC). Lines scans were performed from the outer part (A) to the inner part (B) of the corrosion layer, as depicted by red arrows. (n = 5 line scans/bone compartment/timepoint from 3 independent samples). **c)** corrosion layer thickness measurements from selected CB and IMC zones. **d)** semi-quantitative analyses of the changes of the Ca/P ratio, O, Mg, P, and Ca concentrations (at.%) at bone regions in immediate contact with the corrosion layer at different time points. **e)** The bone-implant contact (BIC) was determined at the cortical bone and intramedullary cavity compartments. Data presented as mean ± standard deviation. (c) n = 110–230 measurements/time point on three independent samples, d) n = 62–85 measurements/time point on three independent samples. (n = 6 regions/time points from 3 independent samples). The Orange dotted line in image a) at 24 weeks denoted the corrosion layer-bone interface. (The figure should be printed in color).

the corrosion medium and high corrosion rate indicated that intense corrosion occurred. However, after 3 days, our *in vitro* data indicated that the pH remained stable to reach 7.9 ± 0.03 at 28 days with the formation of Ca/Mg $(CO_3)_2$ as determined by XPS and the predicted fraction diagrams calculated by Hydra Medusa software. This is consistent with the findings of Lamaka et al. [122] who found a calcium-phosphate/carbonate corrosion layer stable at a pH lower of 8.5. They also highlighted different corrosion rates in immersion solutions containing Ca^{2+} compared to electrolytes solutions without Ca^{2+}, which could be the cause of discrepancies in corrosion rate between our results and previously described results from the ZX00 alloy [44,45].

Comparable to what was observed *in vitro*, the corrosion layers that formed on the ZX00 screws in our *in vivo* studies exhibited a similar composition. The corrosion products were composed of a Mg/O ratio of ~0.5, suggesting the presence of $Mg(OH)_2$, along with the presence of Ca and P indicating the formation of various Ca- and P-containing layers. This is consistent with *in vitro* results previously published investigating Mg–Ca–Zn and low-alloyed Mg–Ca–Zn alloys immersed in the artificial saliva [123], Kokubo's solution [124,125], Hank's solution [126], EBSS, MEM, and MEM supplemented with bovine serum albumin [127]. Similarly, Zhang et al. [121], who implanted Mg-2wt.%Zn-0.5 wt%Ca pins in a rat femoral defect model for 12 weeks, described corrosion products with a chemical composition comparable to our *in vivo* findings. Witte et al. [18] found corrosion layers containing calcium phosphates on 4 different magnesium alloys implanted within the medullary cavity of guinea pig femora. Lee et al. [48] observed changes in elemental composition and crystallinity within the degradation interface when implanted Mg–5Ca–1Zn rods in the femoral condyle of rabbits. According to their findings, a biomimicking calcification matrix was formed at the degrading interface which initiate the bone formation. Additionally, our histology revealed the staining of the corrosion products that resembled bone (dark pink) after 24 weeks of *in vivo* implantation. As previously reported, this pattern is consistent with the Ca- and P-rich degradation layers [18,39,43]. However, although the corrosion layers of ZX00 screws formed during our *in vitro* and *in vivo* tests were composed of the same elements, the corrosion layer thickness and the elemental distribution were different *in vivo*, consistent with some previous studies [40,65,128]. This might be because various screw zones in our *in vivo* study were surrounded by different local environments. The screw's head was often enclosed by the soft tissues (overlying muscle/connective tissue), the shaft was in contact with the cortical bone, and the implant's middle region was exposed to the bone marrow. These distinct tissue compartments (soft tissues, periosteal layer, cortical bone, and medullar cavity) play a role not only in bone

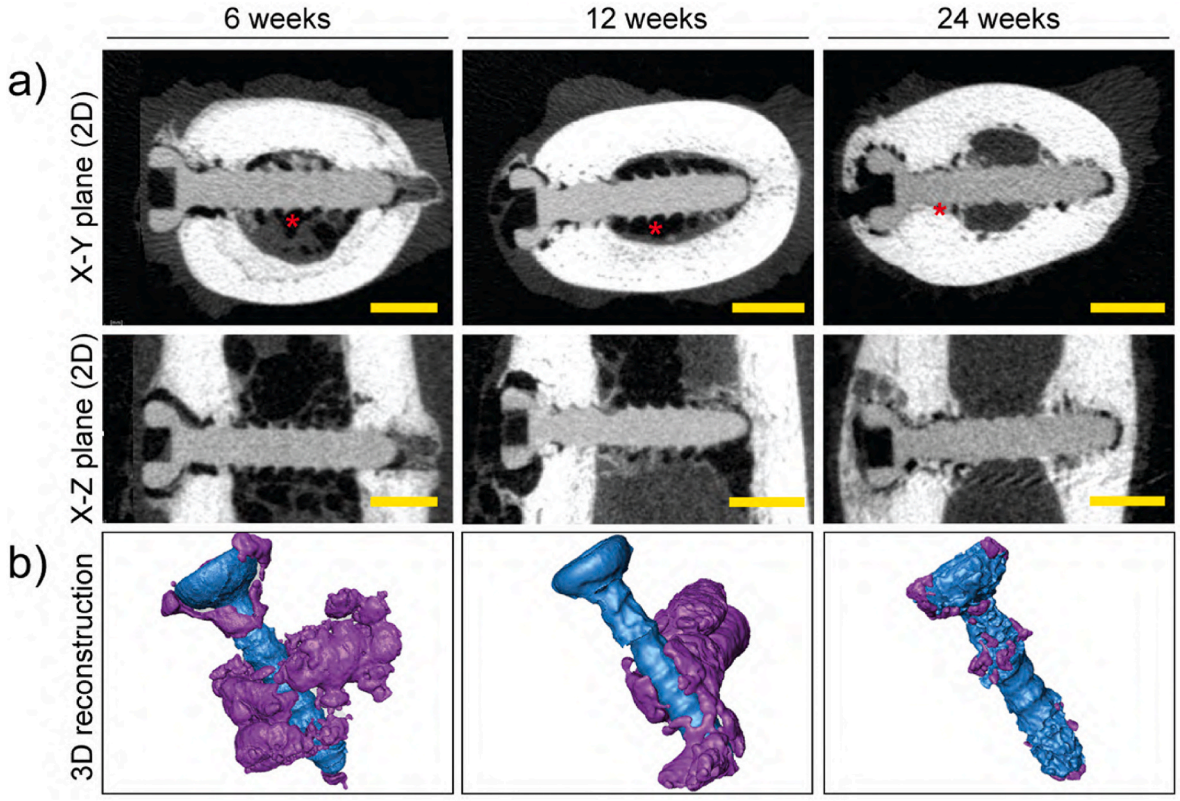

Fig. 11. µCT reconstructions of ZX00 screws after 6-, 12-, and 24- weeks of in vivo implantation. a) µCT reconstructions (2D slices) in the X–Y plane (first row) and the X-Z plane (second row). The radiolucent zones adjacent to the implant screw were gas voids (red asterisks). **b)** 3D model reconstructions of the ZX00 screw (blue color) after 6, 12, and 24 weeks of implantation with surrounding gas cavities (purple color). Scale bar in panel a) is 2 mm. (The figure should be printed in color).

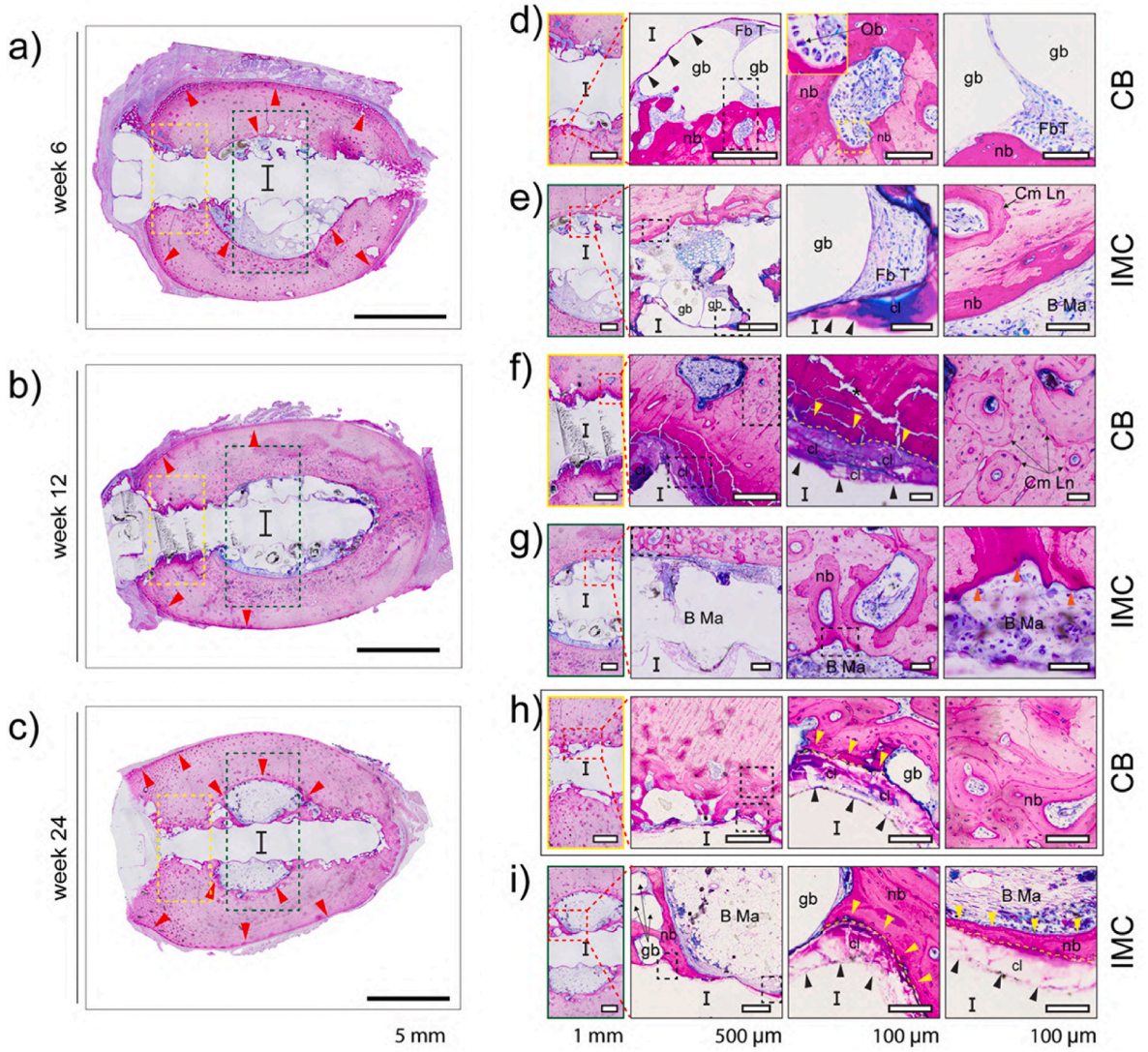

Fig. 12. Representative images of McNeal-stained bone sections after 6- (a, d, e), 12- (b, f, g) and 24- (c, h, i) weeks of *in vivo* implantation. The first column provides an overview of the ZX00 screws after (**a**) 6-, (**b**) 12-, and (**c**) 24- weeks of implantation. CB and IMC compartments are magnified and denoted by yellow and green rectangles, respectively in (**d, e, f, g, h, i**). The red arrows in (**a, b, c**) point to the appositional growth in the periosteum and new bone formation in the endosteum zones. Corrosion products are indicated by black arrows. Tight direct bone contact with the degradation products and new bone formation next to the ZX00 screws is identified by yellow (**f, h, i**) and orange (g) arrows. (I) Site of implant and the following abbreviations used to describe various features: gb (gas bubbles), Ob (osteoblasts), nb (new bone), Fb T (fibrous tissue), *Cm* Ln (cement line), B Ma (bone marrow), cl (corrosion layer), and (*) sample preparation artifact. (The figure should be printed in color).

fracture repair but also causes different degradation at various screw's regions strongly influenced by the environment in which the implant was placed [47,71]. The amplified early inflammatory response in soft tissues [129] combined with hematoma formation and a local decrease in pH [18,130–132] results in a hypoxic and acidic environment when implanting an Mg orthopedic device with a faster degradation of the Mg implant region in contact with soft tissues [17,71,132,133]. However, the accelerated degradation of screw implant's heads observed in soft tissues could be an advantage as faster degradation could avoid soft-tissue irritation. Herber et al. [52] demonstrated that the ZX00 screw's head located in the soft tissue area was predominantly resorbed avoiding shoe conflict for the patients. Moreover, it has been described faster corrosion of Mg-based devices at the medullary cavity, assuming that the accelerated implant degradation is caused by the high blood vessel content and rich supply of body fluids promoting ion exchange between the surrounding tissue and the Mg implant surface [45,61,134–137]. In contrast, the dense mineralized structure of the cortical bone slows down the degradation of Mg implant regions placed in this compartment [17,71]. All factors influencing degradation, including implant location, must be considered when analyzing the degradation layer composition and degradation rate of implants, which makes it difficult to precisely estimate the corrosion rate of Mg implants. Furthermore, the relatively high standard deviation of the plotted corrosion layer thicknesses in our study, which ranged from ~20 µm to 62 µm in the cortical bone and from ~52 to 60 µm in the medullary cavity with regions reaching up to ~174 µm, could be attributed to several factors, including the nature of each sheep (weight, growth, variation in feeding patterns and movement activity) [24,138], which may have influenced differences in their bone healing process, metabolism, and implant degradation.

Previous animal experiments that provide quantitative data revealed that the corrosion layer thicknesses range from 10 to 250 µm [32,39,48,128,134,139–144]. This broad range is a result of the various Mg-based biomaterials implanted, the different animal models and implantation sites, and the various experimental points for observations. In large animal models, Imwinkelried et al. [139] observed a ~30 µm corrosion

products/layer on uncoated WE43 plates implanted subcutaneously on the nasal bones of minipigs for 24 weeks. Grün et al. [32] and Holweg et al. [39] investigated the corrosion behavior of ZX00 screws implanted in lamb tibia bones. After 12 weeks of implantation, histological analysis revealed similar thicknesses (~50 μm and ~43 μm, respectively) of corrosion layers formed on the screw surfaces. This broad range of corrosion layer thickness demonstrated the dependence of Mg corrosion on implant location, making it difficult to precisely estimate the corrosion rate of Mg implant materials. However, our *in vivo* results are of great clinical significance because they resemble real clinical scenarios in which implanted Mg devices are in contact with different tissue compartments that influence each other during Mg-implant degradation. In addition, it is important to consider that although the mechanisms of bone healing with implants are similar to those of bone healing without implants [1], in the *in vivo* environment, the corrosion of Mg-based implants is influenced by a continuous and time-dependent body-response phenomenon involving protein absorption, coagulation and inflammation [11]. This body response varies in each tissue in normal fracture healing where different cellular response evolves. It has been described as a lymphocyte- and granulocyte-rich inflammation in cortical and cancellous bone healing, respectively [145]. Also, Liu et al. [66] found a different modulation of inflammation signaling pathways when pure Mg and AZ31 implants with varied manufacturing processes were implanted for 9 days in the femur of male rats. Hence, further investigations in subsequent *in vivo* studies are required to elucidate the corrosion environment at the cortico-cancellous bone transitional zone and ascertain the influence of Mg-implant degradation in the cellular response of both bone compartments.

As mentioned, our findings show that the screw does not corrode uniformly. The results from the electrochemical measurements proved that the least corrosion-resistant zone of the screw is the head. In this region, the grain size and the distribution of the dislocations were different from those observed in the valley and tip zones. As shown in our previous works [87,97], the Mg's dissolution rate strongly depends on the spatial distribution of the potential on the surface of materials. Mg's dissolution rate is related to the anodic/cathodic sites of corrosion where cathodic reactions must be compensated by anodic reactions. In the case of the screw head, the large primary grains are the cathodic areas surrounded by the small anodic grains. The large cathodic areas drive small grains to dissolve quickly. Considering the screw valley and the tip, the spatial distribution of the half-reactions was more uniform due to more uniform grain size distribution in these screw regions. Also, the higher accumulation of the dislocation density in the head of the screw will promote corrosion reactions. We presumed that the microstructural differences in the screw head compared to the screw valley and tip regions resulted from the manufacturing process. Controlling the microstructure is a key component for modification of the dissolution of Mg screws for potential clinical use. Therefore, the manufacturing process must be carried out with the utmost accuracy. However, it is important to consider also that variations in implantation in our *in vivo* model make it difficult to compare the degradation performance of the screw head and tip. The anatomical variability [146,147] may also contribute to surgical inaccuracies in real-world clinical scenarios. Similar challenges in identifying a representative area for the entire degradation of Mg-based implants *in vivo* have been highlighted previously [65]. Therefore, future *in vivo* animal studies should undertake medical image-based analysis before implantation with the additional support of implant surgical guides, in order to precisely implant a ZX00 screw in the same position, thereby enabling a corrosion performance comparison of the head and tip region of the screw at different time points to determine whether the difference in corrosion observed *in vitro* occurs *in vivo* in these screw zones.

Previous *in vivo* studies have revealed that hydrogen gas evolution is primarily found adjacent to Mg–Zn–Ca implants investigated [17,32,39,43,44,148,149]. Although the composition and volume of the released gas during ZX00 alloy degradation were not investigated in this study, our μCT and histology findings after 6 weeks of implantation revealed numerous gas voids mainly in the intramedullary cavity. These gas cavities were visible up to 12 weeks post-implantation, supporting previous findings [32,45]. After 24 weeks of implantation, corrosion reactions were not as intense. At this time point, the gas cavities in the cortical bone compartment were considerably smaller, suggesting that ZX00 alloy corrosion slowed over this period. Depending on the local gas saturation, this gas may cause irritation, cell and tissue displacement [137], accumulation in tissue cavities [135,150], mechanical disturbance that may disrupt the initial cortical bone healing process, resulting in callus formation [17], or altering the trabecular bone structure [46]. In the case of H_2 released in soft tissues, large gas voids can be formed, and the H_2 concentration can be permeated through the skin [151], eliminated by the local blood flow [137] or removed by puncture with a syringe as reported in small [18] and large animal studies [152]. When pure Mg was subcutaneously implanted in Sprague-Dawley® (SD) rats, Ben Amara et al. [129] observed that the H_2 accumulation accompanied the amplified early inflammatory response. In contrast, Zhang et al. [134], who implanted Mg–Zn–Mn pins did not observe gas voids in soft tissues 5 weeks after implantation owing to the alloy's gradual degradation. However, gas voids probably dissipated through absorption in the surrounding tissue [132] and were not visible at the time point of experimental observation.

Similarly, gas cavities have been observed in Mg implants exposed to the intramedullary cavity in small and large animal models. Transcortical implantation of XHP-Mg pins versus ZX00 pins in the diaphysis of SD rats resulted in moderate gas evolution that was more pronounced for XHP Mg pins already at 2 weeks [44], whereas increased gas formation and enhanced implant volume loss due to faster degradation was observed around ZX00 pins also transcortical implanted in the tibia of ovariectomy-induced osteoporotic rats. Osteoporotic bone has decreased mineralization [43] and deteriorated bone microarchitecture [153,154]. Marek et al. [46] observed gas surrounding ZX00 intramedullary nails at the proximal epiphysis with an increased gas volume at 2 weeks which decreased up to 76 weeks causing bone-structure alterations in the initial phase of ZX00 degradation. As the bone marrow cavity is highly perfused by blood vessels, the water content and local blood flow around the implants influenced not only the accelerated corrosion of Mg implants at this bone compartment but also the local diffusion and solubility of H_2, which contributed to the gas transport and absorption by the vascular system, reducing the size of the gas pockets [17,45,155,156].

In contrast to what has been reported regarding the gradual disappearance of gas bubbles as the implantation time increases as observed in our study, Wang et al. [157] observed an increased density of the gas bubbles after 24 weeks around the Mg–Zn–Zr pins implanted into the femoral condyles of Japanese white rabbits. The femoral condyle is composed of bone marrow, spongy bone, compact bone and cartilage [71], and is a region of high blood flow that could contribute to rapid corrosion of the alloy, which would explain the number of gas cavities the authors observed at the experimental time point. According to their findings, the degradation of Mg–Zn–Zr alloy caused gas cavitation within the cancellous bone, which was progressively filled with newly regenerated bone, cartilage, and fibrous connective tissues. Han et al. [47] , who implanted Mg5Ca pins in the femoral condyle of SD rats, observed insufficient bone healing and low-density tissue adjacent to the implants, indicating the possible fibrotic tissue formation due to the alloy's rapid degradation accompanied by metallic ions and hydrogen gas release. With W4 interferences screws implanted in the femoral condyle of sheep, Thormann et al. [158] also observed implant loosening, delayed osseointegration, and a significant amount of gas evolution. After 6 weeks, gas voids were observed surrounding the entire implant and spreading in the trabecular bone; after 12 weeks, the voids were surrounded by soft tissue. In addition, they observed a large number of multinuclear cells and blood vessels in close proximity to the gas cavities, indicating an endeavor by the tissue to control the gas

evolution. However, after 12 weeks the number of vessels decreased, indicating a reduced effort by tissue to regulate the gas released. Thus, this gas formation ascribed to the hydrogen evolution during Mg corrosion [159] is proportional to the Mg alloy's rate of degradation, the implant location, and the selected animal model [155,160]. Nevertheless, H_2 may not be the sole gas present in the gas cavities. Before implantation, the body fluid contains dissolved nitrogen (N_2), oxygen (O_2) and carbon dioxide (CO_2) in proportion to their partial pressure. When an Mg device is implanted, corrosion reactions generate H_2 with a proportionate increase in H_2 pressure. As previously demonstrated [156], this H_2 is dissolved and/or diffused through the vascular system while being exchanged with the undissolved N_2, O_2 and CO_2 gases present in the voids [159]. Hence, the chemical composition of the Mg-based alloy, the implant location in the body, and the time points selected for observations may account for differences in the generation and dissolution of the gas voids. However, in our study, despite the degradation reactions and gas formation, new bone in direct contact with corrosion products was formed demonstrating that the ZX00 alloy did not cause adverse effects in the surrounding tissues, promoting osteogenesis and bone healing consistent with previously reported studies [17,32,39,40,45,157]. Nevertheless, the specific composition and effects of the gas produced by the degradation of the ZX00 alloy are still not fully understood and need to be clarified in future studies.

Additionally, implant integrity is crucial during the initial fracture-healing stage to provide sufficient stability for the reduction and fixation of bone fracture fragments [1,40]. To provide sufficient primary fracture stabilization, the corrosion behavior of Mg-based implants should match the healing time of a bone fracture. This mechanical integrity must be maintained for 4–6 weeks in children and 12–18 weeks in adults [44,137]. The majority of fractures involving the clavicle, hand, wrist and distal radius fractures require 4–8 weeks of mechanical support, whereas femur fractures and femoral neck fractures required 8–14 and 12–24 weeks of healing time, respectively [41]. Our results found that the main body of the ZX00 screw slowly degraded and still was present after 24 weeks of implantation. Lee et al. [48] demonstrated that 4–6 weeks of mechanical support for bone-healing was required when Mg-5wt.% Ca-1wt.% Zn was implanted to treat wrist and hand fractures. Castellani et al. [30] observed a similar outcome after implanting Mg-RE alloy rods in the femoral bone of Sprague-Dawley rats for up to 24 weeks. Holweg et al. [39] also found fracture consolidation without impairment in a juvenile sheep model using ZX00 osteosynthesis screws which still were discernible after 12 weeks. In contrast, Bian et al. [161] observed that Mg-1.8Zn-0.2Gd pins implanted in the tibia of rats, the pins maintained their shape for the first 2 months before degrading nearly completely after 6 months of implantation. In the cortical zone, the implant was directly integrated with the bone, whereas in the medullary cavity, some trabecular bones were in contact with the implant and some trabecular bones were found at a certain distance to the implant. They attributed the accelerated degradation to the mildly localized corrosion observed *in vivo*, which was ascribed to the alloy's inhomogeneous composition and impurities introduced during the production processes. This demonstrates how crucial is to have consistent manufacturing methods to prevent the introduction of impurities and the continuous monitoring of the microstructure of Mg implants to ensure homogeneous composition throughout the entire Mg implant geometry for those intended for biomedical applications. Based on our SEM, histology and BIC findings, ZX00 screws provide sufficient long-term fixation for adequate bone healing and mechanical strength.

5. Conclusion

Based on the results presented in this study the following conclusions can be drawn.

- The corrosion performance of the screws produced from ZX00 alloys was investigated under *in vitro* and *in vivo* conditions, and the results from both methods were complementary. Although the corrosion layers formed under *in vitro* and *in vivo* conditions had the same elemental composition, the elemental distribution and thickness of the corrosion layers varied. This indicated that the degradation mechanisms occurring under physiological conditions are highly dependent on the surrounding environment to which the implants are exposed. Consequently, *in vitro* tests must be further improved. This confirms that replicating the exact conditions of *in vivo* testing is difficult to achieve through *in vitro* testing. Therefore, improving *in vitro* experimental design is of critical importance to reduce *in vivo* trials.
- Until 28 days of immersion under physiological conditions, the corrosion rate calculated based on *in vitro* methods increased continuously.
- The corrosion rate of ZX00 after *in vitro* testing was slower (1.04 mm $\times$ year^{-1}) when compared to the alloys with higher Zn concentration (ZX10, ZX20, and ZX50).
- The technological aspect of screw manufacturing is important from a materials design point of view. Our results clearly indicate that the ZX00 screw corroded nonuniformly, and the zones of the screw with the uniform grain size distribution had the lowest degradation rate. Therefore, controlling microstructure is a key parameter that can be used to tune the dissolution of Mg screws under physiological conditions.
- The vast number of voids observed i*n vivo* 6 weeks after implantation was indicative of gas produced by the degradation of the ZX00 screw, predominantly within the intramedullary cavity. As the implantation time increased, the observed voids were smaller in size. This size reduction over time may be due to the exchange mechanism of water content and blood flow in the surrounding tissues and does not necessarily indicate the deceleration of the corrosion mechanisms.
- Despite the corrosion reactions and gas release during the ZX00 screw degradation, new bone formed in direct contact with corrosion products without any adverse effects in the surrounding tissues. Therefore, ZX00 alloy is a potential Mg-based alloy to consider for temporary bone implants.

Ethical approval

The large animal trial (Permit number: BMBWF-66.010-0107-V-3b-2019) was approved by the Austrian Federal Ministry for Science and Research and followed the guidelines for the accommodation and care of animals formulated by the European Convention for the protection of vertebrate animals used for experimental and other scientific purposes. The experiment was performed according to the 3R principles (replace, reduce, and refine).

CRediT authorship contribution statement

Diana C. Martinez: Conceptualization, Methodology, Investigation, Formal analysis, Visualization, Writing – original draft, Writing – review & editing. **Anna Dobkowska:** Investigation, Formal analysis, Writing – original draft, Writing – review & editing. **Romy Marek:** Methodology, Investigation. **Hanna Ćwieka:** Investigation, Formal analysis. **Jakub Jaroszewicz:** Formal analysis. **Tomasz Płociński:** Supervision, Writing – review & editing. **Črtomir Donik:** Investigation. **Heike Helmholz:** Writing – review & editing. **Bérengère Luthringer-Feyerabend:** Writing – review & editing. **Berit Zeller-Plumhoff:** Supervision, of Hanna Ćwieka, Writing – review & editing. **Regine Willumeit-Römer:** Supervision, Writing – review & editing, Funding acquisition. **Wojciech Święszkowski:** Conceptualization, Supervision, Writing – review & editing, Funding acquisition.

Declaration of competing interest

The author(s) has disclosed no potential conflicts of interest

regarding this article's research, authorship, and/or publication.

Acknowledgements

This research was carried out within the project "Promoting safety by a novel combination of imaging technologies for biodegradable magnesium implants, MgSafe" which is funded by the European Union's Horizon 2020 Marie Skłodowska-Curie Action (MSCA) (grant number No. 811226). Also, this research was funded under statutory work at the Faculty of Materials Science and Engineering Warsaw University of Technology in Poland. The authors gratefully acknowledge the support during *in vitro* experiments to Monika Luczak from the Institute of Metallics Biomaterials, Helmholtz-Zentrum Hereon GmbH, Geesthacht, Germany, and the technical assistance in the preparation and histological processing of explants by Uwe Schwarze from the Department of Dental Medicine and Oral Health, and the Department of Orthopaedics and Traumatology, Medical University of Graz, Austria.

Appendix A. Supplementary data

Supplementary data to this article can be found online at https://doi.org/10.1016/j.bioactmat.2023.05.004.

References

[1] T. Kim, C.W. See, X. Li, D. Zhu, Orthopedic implants and devices for bone fractures and defects: past, present and perspective, Eng. Regen. 1 (2020) 6–18, https://doi.org/10.1016/j.engreg.2020.05.003.
[2] W. Jin, P.K. Chu, Orthopedic Implants, Elsevier Inc., 2019, https://doi.org/10.1016/B978-0-12-801238-3.10999-7.
[3] M. Chagnon, L.G. Guy, N. Jackson, Evaluation of magnesium-based medical devices in preclinical studies: challenges and points to consider, Toxicol. Pathol. 47 (2019) 390–400, https://doi.org/10.1177/0192623318816936.
[4] A. Goharian, M.R.A. Kadir, M.R. Abdullah, Biodegradable Metals (Biodegradable Magnesium Alloys), Elsevier Inc., 2017, https://doi.org/10.1016/B978-0-12-804634-0.00008-2.
[5] N. Shayesteh Moghaddam, M. Taheri Andani, A. Amerinatanzi, C. Haberland, S. Huff, M. Miller, M. Elahinia, D. Dean, Metals for bone implants: safety, design, and efficacy, Biomanufacturing Rev 1 (2016) 1–16, https://doi.org/10.1007/s40898-016-0001-2.
[6] O. Bazaka, K. Bazaka, P. Kingshott, R.J. Crawford, E.P. Ivanova, in: Christopher Spi (Ed.), Chapter 1. Metallic Implants for Biomedical Applications, Chem. Inorg. Biomater., 2021, pp. 1–98, https://doi.org/10.1039/9781788019828-00001.
[7] J.M. Lane, J.E. Mait, A. Unnanuntana, B.P. Hirsch, A.D. Shaffer, O.A. Shonuga, 6.616 - materials in fracture fixation, in: P.B.T.-C.B. Ducheyne (Ed.), Comprenhensive Biomater., Elsevier, Oxford, 2011, pp. 219–235, https://doi.org/10.1016/B978-0-08-055294-1.00251-8.
[8] L. Elkaiam, O. Hakimi, G. Yosafovich-Doitch, S. Ovadia, E. Aghion, Correction to: in vivo evaluation of Mg–5%Zn–2%Nd alloy as an innovative biodegradable implant material, Ann. Biomed. Eng. 47 (2019) 2515, https://doi.org/10.1007/s10439-019-02378-y.
[9] Y. Li, C. Wen, D. Mushahary, R. Sravanthi, N. Harishankar, G. Pande, P. Hodgson, Mg-Zr-Sr alloys as biodegradable implant materials, Acta Biomater. 8 (2012) 3177–3188, https://doi.org/10.1016/j.actbio.2012.04.028.
[10] S. Amukarimi, M. Mozafari, Biodegradable magnesium-based biomaterials: an overview of challenges and opportunities, MedComm 2 (2021) 123–144, https://doi.org/10.1002/mco2.59.
[11] H. Hermawan, Updates on the research and development of absorbable metals for biomedical applications, Prog. Biomater. 7 (2018) 93–110, https://doi.org/10.1007/s40204-018-0091-4.
[12] C. Liu, Z. Ren, Y.D. Xu, S. Pang, X.B. Zhao, Y. Zhao, Biodegradable magnesium alloys developed as bone repair materials: a review, Scanning (2018) 2018, https://doi.org/10.1155/2018/9216314.
[13] Z. Zeng, N. Stanford, C.H.J. Davies, J.F. Nie, N. Birbilis, Magnesium extrusion alloys: a review of developments and prospects, Int. Mater. Rev. 64 (2019) 27–62, https://doi.org/10.1080/09506608.2017.1421439.
[14] P.-R. Cha, H.-S. Han, G.-F. Yang, Y.-C. Kim, K.-H. Hong, S.-C. Lee, J.-Y. Jung, J.-P. Ahn, Y.-Y. Kim, S.-Y. Cho, J.Y. Byun, K.-S. Lee, S.-J. Yang, H.-K. Seok, Biodegradability engineering of biodegradable Mg alloys: tailoring the electrochemical properties and microstructure of constituent phases, Sci. Rep. 3 (2013) 2367, https://doi.org/10.1038/srep02367.
[15] S. Agarwal, J. Curtin, B. Duffy, S. Jaiswal, Biodegradable magnesium alloys for orthopaedic applications: a review on corrosion, biocompatibility and surface modifications, Mater. Sci. Eng. C 68 (2016) 948–963, https://doi.org/10.1016/j.msec.2016.06.020.
[16] J. Zhang, Y. Jiang, Z. Shang, B. Zhao, M. Jiao, W. Liu, M. Cheng, B. Zhai, Y. Guo, B. Liu, X. Shi, B. Ma, Biodegradable metals for bone defect repair: a systematic review and meta-analysis based on animal studies, Bioact. Mater. 6 (2021) 4027–4052, https://doi.org/10.1016/j.bioactmat.2021.03.035.
[17] T. Kraus, S.F. Fischerauer, A.C. Hanzi, P.J. Uggowitzer, J.F. Loffler, A. M. Weinberg, Magnesium alloys for temporary implants in osteosynthesis: in vivo studies of their degradation and interaction with bone, Acta Biomater. 8 (2012) 1230–1238, https://doi.org/10.1016/j.actbio.2011.11.008.
[18] F. Witte, V. Kaese, H. Haferkamp, E. Switzer, A. Meyer-Lindenberg, C.J. Wirth, H. Windhagen, In vivo corrosion of four magnesium alloys and the associated bone response, Biomaterials 26 (2005) 3557–3563, https://doi.org/10.1016/j.biomaterials.2004.09.049.
[19] S. Chen, S.K. Guan, W. Li, H.X. Wang, J. Chen, Y.S. Wang, H.T. Wang, In vivo degradation and bone response of a composite coating on Mg-Zn-Ca alloy prepared by microarc oxidation and electrochemical deposition, J. Biomed. Mater. Res. Part B-Applied Biomater. 100B (2012) 533–543, https://doi.org/10.1002/jbm.b.31982.
[20] M. Razavi, M. Fathi, O. Savabi, D. Vashaee, L. Tayebi, In vivo biocompatibility of Mg implants surface modified by nanostructured merwinite/PEO, J. Mater. Sci. Med. 26 (2015), https://doi.org/10.1007/s10856-015-5514-3.
[21] S.A. Abdel-Gawad, M.A. Shoeib, Corrosion studies and microstructure of Mg - Zn - Ca alloys for biomedical applications, Surface. Interfac. 14 (2019) 108–116, https://doi.org/10.1016/j.surfin.2018.11.011.
[22] Z.R. Qi, Q. Zhang, L.L. Tan, X. Lin, Y. Yin, X.L. Wang, K. Yang, Y. Wang, Comparison of degradation behavior and the associated bone response of ZK60 and PLLA in vivo, J. Biomed. Mater. Res., Part A 102 (2014) 1255–1263, https://doi.org/10.1002/jbm.a.34795.
[23] H. Chai, L. Guo, X. Wang, X. Gao, K. Liu, Y. Fu, J. Guan, L. Tan, K. Yang, In vitro and in vivo evaluations on osteogenesis and biodegradability of a β-tricalcium phosphate coated magnesium alloy, J. Biomed. Mater. Res., Part A 100 A (2012) 293–304, https://doi.org/10.1002/jbm.a.33267.
[24] J. Hofstetter, E. Martinelli, S. Pogatscher, P. Schmutz, E. Povoden-Karadeniz, A. M. Weinberg, P.J. Uggowitzer, J.F. Löffler, Influence of trace impurities on the in vitro and in vivo degradation of biodegradable Mg-5Zn-0.3Ca alloys, Acta Biomater. 23 (2015) 347–353, https://doi.org/10.1016/j.actbio.2015.05.004.
[25] F. Rosalbino, S. De Negri, A. Saccone, E. Angelini, S. Delfino, Bio-corrosion characterization of Mg-Zn-X (X = Ca, Mn, Si) alloys for biomedical applications, J. Mater. Sci. Mater. Med. 21 (2010) 1091–1098, https://doi.org/10.1007/s10856-009-3956-1.
[26] W.D. Mueller, M. Lucia Nascimento, M.F. Lorenzo De Mele, Critical discussion of the results from different corrosion studies of Mg and Mg alloys for biomaterial applications, Acta Biomater. 6 (2010) 1749–1755, https://doi.org/10.1016/j.actbio.2009.12.048.
[27] N.T. Kirkland, J. Lespagnol, N. Birbilis, M.P. Staiger, A survey of bio-corrosion rates of magnesium alloys, Corrosion Sci. 52 (2010) 287–291, https://doi.org/10.1016/j.corsci.2009.09.033.
[28] K. Chen, J. Dai, X. Zhang, Improvement of corrosion resistance of magnesium alloys for biomedical applications, Corrosion Rev. 33 (2015) 101–117, https://doi.org/10.1515/corrrev-2015-0007.
[29] R. Radha, D. Sreekanth, Insight of magnesium alloys and composites for orthopedic implant applications – a review, J. Magnesium Alloys 5 (2017) 286–312, https://doi.org/10.1016/j.jma.2017.08.003.
[30] C. Castellani, R.A. Lindtner, P. Hausbrandt, E. Tschegg, S.E. Stanzl-Tschegg, G. Zanoni, S. Beck, A.-M.M. Weinberg, Bone-implant interface strength and osseointegration: biodegradable magnesium alloy versus standard titanium control, Acta Biomater. 7 (2011) 432–440, https://doi.org/10.1016/j.actbio.2010.08.020.
[31] T. Sato, Y. Shimizu, K. Odashima, Y. Sano, A. Yamamoto, T. Mukai, N. Ikeo, T. Takahashi, H. Kumamoto, In vitro and in vivo analysis of the biodegradable behavior of a magnesium alloy for biomedical applications, Dent, Mater. J. 38 (2019) 11–21, https://doi.org/10.4012/dmj.2017-324.
[32] N.G. Grün, P. Holweg, S. Tangl, J. Eichler, L. Berger, J.J.J.P. van den Beucken, J. F. Löffler, T. Klestil, A.M. Weinberg, Comparison of a resorbable magnesium implant in small and large growing-animal models, Acta Biomater. 78 (2018) 378–386, https://doi.org/10.1016/j.actbio.2018.07.044.
[33] D.T. Chou, D. Hong, P. Saha, J. Ferrero, B. Lee, Z. Tan, Z. Dong, P.N. Kumta, In vitro and in vivo corrosion, cytocompatibility and mechanical properties of biodegradable Mg-Y-Ca-Zr alloys as implant materials, Acta Biomater. 9 (2013) 8518–8533, https://doi.org/10.1016/j.actbio.2013.06.025.
[34] R.S. Park, Y.K. Kim, S.J. Lee, Y.S. Jang, I.S. Park, Y.H. Yun, T.S. Bae, M.H. Lee, Corrosion behavior and cytotoxicity of Mg-35Zn-3Ca alloy for surface modified biodegradable implant material, J. Biomed. Mater. Res. Part B-Applied Biomater. 100B (2012) 911–923, https://doi.org/10.1002/jbm.b.32652.
[35] H. Miao, D. Zhang, C. Chen, L. Zhang, J. Pei, Y. Su, H. Huang, Z. Wang, B. Kang, W. Ding, H. Zeng, G. Yuan, Research on biodegradable Mg-Zn-Gd alloys for potential orthopedic implants: in vitro and in vivo evaluations, ACS Biomater. Sci. Eng. 5 (2019) 1623–1634, https://doi.org/10.1021/acsbiomaterials.8b01563.
[36] H. Kabir, K. Munir, C. Wen, Y. Li, Recent research and progress of biodegradable zinc alloys and composites for biomedical applications: biomechanical and biocorrosion perspectives, Bioact. Mater. 6 (2021) 836–879, https://doi.org/10.1016/j.bioactmat.2020.09.013.
[37] Y. Lu, A.R. Bradshaw, Y.L. Chiu, I.P. Jones, Effects of secondary phase and grain size on the corrosion of biodegradable Mg-Zn-Ca alloys, Mater. Sci. Eng. C-Materials Biol. Appl. 48 (2015) 480–486, https://doi.org/10.1016/j.msec.2014.12.049.
[38] L.H.C. Becerra, M.A.L.H. Rodríguez, H. Esquivel-Solís, R.L. Arroyo, A.T. Castro, Bio-inspired biomaterial Mg–Zn–Ca: a review of the main mechanical and

biological properties of Mg-based alloys, Biomed. Phys. Eng. Express. 6 (2020), 42001, https://doi.org/10.1088/2057-1976/ab9426.
[39] P. Holweg, L. Berger, M. Cihova, N. Donohue, B. Clement, U. Schwarze, N. G. Sommer, G. Hohenberger, J.J.J.P. van den Beucken, F. Seibert, A. Leithner, J. F. Löffler, A.M. Weinberg, A lean magnesium–zinc–calcium alloy ZX00 used for bone fracture stabilization in a large growing-animal model, Acta Biomater. 113 (2020) 646–659, https://doi.org/10.1016/j.actbio.2020.06.013.
[40] M. Cihova, E. Martinelli, P. Schmutz, A. Myrissa, R. Schäublin, A. Weinberg, P. Uggowitzer, J.F. Löffler, The role of zinc in the biocorrosion behavior of resorbable Mg−Zn−Ca alloys, Acta Biomater. (2019), https://doi.org/10.1016/j.actbio.2019.09.021.
[41] G. Mao, X. Jin, J. Sun, X. Han, M. Zeng, Y. Qiu, W. Bian, Microalloying design of biodegradable Mg-2Zn-0.05Ca promises improved bone-implant applications, ACS Biomater. Sci. Eng. 7 (2021) 2755–2766, https://doi.org/10.1021/acsbiomaterials.1c00218.
[42] Y. Jang, Z. Tan, C. Jurey, Z. Xu, Z. Dong, B. Collins, Y. Yun, J. Sankar, Understanding corrosion behavior of Mg-Zn-Ca alloys from subcutaneous mouse model: effect of Zn element concentration and plasma electrolytic oxidation, Mater. Sci. Eng. C 48 (2015) 28–40, https://doi.org/10.1016/j.msec.2014.11.029.
[43] N.G. Sommer, D. Hirzberger, L. Paar, L. Berger, H. Ćwieka, U.Y. Schwarze, V. Herber, B. Okutan, A.J. Bodey, R. Willumeit-Römer, B. Zeller-Plumhoff, J. F. Löffler, A.M. Weinberg, Implant degradation of low-alloyed Mg–Zn–Ca in osteoporotic, old and juvenile rats, Acta Biomater. 147 (2022) 427–438, https://doi.org/10.1016/j.actbio.2022.05.041.
[44] B. Okutan, U.Y. Schwarze, L. Berger, D.C. Martinez, V. Herber, O. Suljevic, T. Plocinski, W. Swieszkowski, S.G. Santos, A.M. Weinberg, N.G. Sommer, R. Schindl, Biomaterials Advances the Combined Effect of Zinc and Calcium on the Biodegradation of Ultrahigh-Purity Magnesium Implants, 2023, p. 146, https://doi.org/10.1016/j.bioadv.2023.213287.
[45] R. Marek, H. Ćwieka, N. Donohue, P. Holweg, J. Moosmann, F. Beckmann, I. Brcic, U.Y. Schwarze, K. Iskhakova, M. Chaabane, S. Sefa, B. Zeller-Plumhoff, A. M. Weinberg, R. Willumeit-Römer, N.G. Sommer, Degradation behavior and osseointegration of Mg-Zn-Ca screws in different bone regions of growing sheep—a pilot study, Regen. Biomater. (2022), https://doi.org/10.1093/rb/rbac077 rbac077.
[46] R. Marek, J. Eichler, U.Y. Schwarze, S. Fischerauer, O. Suljevic, L. Berger, J. F. Löffler, P.J. Uggowitzer, A.-M. Weinberg, Long-term in vivo degradation of Mg–Zn–Ca elastic stable intramedullary nails and their influence on the physis of juvenile sheep, Biomater. Adv. (2023), 213417, https://doi.org/10.1016/j.bioadv.2023.213417.
[47] H.S. Han, I. Jun, H.K. Seok, K.S. Lee, K. Lee, F. Witte, D. Mantovani, Y.C. Kim, S. Glyn-Jones, J.R. Edwards, Biodegradable magnesium alloys promote angio-osteogenesis to enhance bone repair, Adv. Sci. 7 (2020) 1–12, https://doi.org/10.1002/advs.202000800.
[48] J.-W. Lee, H.-S. Han, K.-J. Han, J. Park, H. Jeon, M.-R. Ok, H.-K. Seok, J.-P. Ahn, K.E. Lee, D.-H. Lee, S.-J. Yang, S.-Y. Cho, P.-R. Cha, H. Kwon, T.-H. Nam, J.H. Lo Han, H.-J. Rho, K.-S. Lee, Y.-C. Kim, D. Mantovani, Long-term clinical study and multiscale analysis of in vivo biodegradation mechanism of Mg alloy, Proc. Natl. Acad. Sci. USA 113 (2016) 716–721, https://doi.org/10.1073/PNAS.1518238113.
[49] J.L. Wang, J.K. Xu, C. Hopkins, D.H.K. Chow, L. Qin, Biodegradable magnesium-based implants in orthopedics—a general review and perspectives, Adv. Sci. 7 (2020), https://doi.org/10.1002/advs.201902443.
[50] D. Zhao, S. Huang, F. Lu, B. Wang, L. Yang, L. Qin, K. Yang, Y. Li, W. Li, W. Wang, S. Tian, X. Zhang, W. Gao, Z. Wang, Y. Zhang, X. Xie, J. Wang, J. Li, Vascularized bone grafting fixed by biodegradable magnesium screw for treating osteonecrosis of the femoral head, Biomaterials 81 (2016) 84–92, https://doi.org/10.1016/j.biomaterials.2015.11.038.
[51] H. Windhagen, K. Radtke, A. Weizbauer, J. Diekmann, Y. Noll, U. Kreimeyer, R. Schavan, C. Stukenborg-Colsman, H. Waizy, Biodegradable magnesium-based screw clinically equivalent to titanium screw in hallux valgus surgery: short term results of the first prospective, randomized, controlled clinical pilot study, Biomed. Eng. Online 12 (2013) 62, https://doi.org/10.1186/1475-925X-12-62.
[52] V. Herber, V. Labmayr, N.G. Sommer, R. Marek, U. Wittig, A. Leithner, F. Seibert, P. Holweg, Can hardware removal be avoided using bioresorbable Mg-Zn-Ca screws after medial malleolar fracture fixation? Mid-term results of a first-in-human study, Injury 53 (2022) 1283–1288, https://doi.org/10.1016/j.injury.2021.10.025.
[53] C. Plaass, C. von Falck, S. Ettinger, L. Sonnow, F. Calderone, A. Weizbauer, J. Reifenrath, L. Claassen, H. Waizy, K. Daniilidis, C. Stukenborg-Colsman, H. Windhagen, Bioabsorbable magnesium versus standard titanium compression screws for fixation of distal metatarsal osteotomies - 3 year results of a randomized clinical trial, J. Orthop. Sci. 23 2 (2018) 321–327, https://doi.org/10.1016/j.jos.2017.11.005.
[54] M. Baldini, V. Coppa, D. Falcioni, G. Cusano, D. Massetti, M. Marinelli, A. P. Gigante, Resorbable magnesium screws for fixation of medial epicondyle avulsion fractures in skeletally immature patients: a comparison with Kirschner wires, J. Child. Orthop. 16 (2022) 481–487, https://doi.org/10.1177/18632521221136100.
[55] H. May, Y.A. Katı, G. Gumussuyu, T.Y. Emre, M. Unal, O. Kose, Bioabsorbable magnesium screw versus conventional titanium screw fixation for medial malleolar fractures, J. Orthop. Traumatol. 21 (2020), https://doi.org/10.1186/s10195-020-00547-7.
[56] C. Sukotjo, T.J. Lima-Neto, J.F.S. Júnior, L. Faverani, M. Miloro, Is there a role for absorbable metals in surgery? A systematic review and meta-analysis of Mg/Mg alloy based implants, Materials 13 (2020), https://doi.org/10.3390/ma13183914.
[57] B. Acar, O. Kose, A. Turan, M. Unal, Y. alper Katı, F. Guler, Comparison of bioabsorbable magnesium versus titanium screw fixation for modified distal chevron osteotomy in hallux valgus, BioMed Res. Int. 2018 (2018), https://doi.org/10.1155/2018/5242806.
[58] A. Wichelhaus, J. Emmerich, T. Mittlmeier, A case of implant failure in partial wrist fusion applying magnesium-based headless bone screws, Case Rep. Orthop. (2016), https://doi.org/10.1155/2016/7049130, 2016.
[59] R. Meier, M. Panzica, Erste Ergebnisse mit einer resorbierbaren MgYREZr-Kompressionsschraube bei der instabilen Kahnbeinfraktur zeigen eine massive Zystenbildung, Handchir. Mikrochir. Plast. Chir. 49 (2017) 37–41, https://doi.org/10.1055/S-0042-121416.
[60] D. Dziuba, A. Meyer-Lindenberg, J.M. Seitz, H. Waizy, N. Angrisani, J. Reifenrath, Long-term in vivo degradation behaviour and biocompatibility of the magnesium alloy ZEK100 for use as a biodegradable bone implant, Acta Biomater. 9 (2013) 8548–8560, https://doi.org/10.1016/j.actbio.2012.08.028.
[61] L.P. Xu, G.N. Yu, E. Zhang, F. Pan, K. Yang, In vivo corrosion behavior of Mg-Mn-Zn alloy for bone implant application, J. Biomed. Mater. Res., Part A 83A (2007) 703–711, https://doi.org/10.1002/jbm.a.31273.
[62] A. Kopp, H. Fischer, A.P. Soares, K. Schmidt-Bleek, C. Leber, H. Kreiker, G. Duda, N. Kröger, K. van Gaalen, H. Hanken, O. Jung, R. Smeets, M. Heiland, C. Rendenbach, Long-term in vivo observations show biocompatibility and performance of ZX00 magnesium screws surface-modified by plasma-electrolytic oxidation in Göttingen miniature pigs, Acta Biomater. 157 (2023) 720–733, https://doi.org/10.1016/j.actbio.2022.11.052.
[63] I. Antoniac, M. Miculescu, V. Mănescu, A. Stere, P.H. Quan, G. Pältânea, A. Robu, K. Earar, Magnesium-based alloys used in orthopedic surgery, Materials 15 (2022) 1–32, https://doi.org/10.3390/ma15031148.
[64] S. Saha, W. Lestari, C. Dini, M.N. Sarian, H. Hermawan, V.A.R. Barão, C. Sukotjo, C. Takoudis, Corrosion in Mg-alloy biomedical implants- the strategies to reduce the impact of the corrosion inflammatory reaction and microbial activity, J. Magnesium Alloys 10 (2022) 3306–3326, https://doi.org/10.1016/j.jma.2022.10.025.
[65] I. Marco, A. Myrissa, E. Martinelli, F. Feyerabend, R. Willumeit-Römer, A. M. Weinberg, O. Van der Biest, In vivo and in vitro degradation comparison of pure Mg, Mg-10Gd and Mg-2Ag: a short term study, Eur. Cell. Mater. 33 (2017) 90–104, https://doi.org/10.22203/eCM.v033a07.
[66] X. Liu, G. Chen, X. Zhong, T. Wang, X. He, W. Yuan, P. Zhang, Y. Liu, D. Cao, S. Chen, K. ichi Manabe, Z. Jiang, T. Furushima, D. Kent, Y. Chen, G. Ni, M. Gao, H. Li, Degradation of differently processed Mg-based implants leads to distinct foreign body reactions (FBRs) through dissimilar signaling pathways, J. Magnesium Alloys (2022), https://doi.org/10.1016/j.jma.2022.03.017.
[67] O. Suljevic, S.F. Fischerauer, A.M. Weinberg, N.G. Sommer, Immunological reaction to magnesium-based implants for orthopedic applications. What do we know so far? A systematic review on in vivo studies, Mater. Today Bio. 15 (2022), 100315, https://doi.org/10.1016/j.mtbio.2022.100315.
[68] R.M. Grzeskowiak, J. Schumacher, M.S. Dhar, D.P. Harper, P.Y. Mulon, D. E. Anderson, Bone and cartilage interfaces with orthopedic implants: a literature review, Front. Surg. 7 (2020) 1–15, https://doi.org/10.3389/fsurg.2020.601244.
[69] P.J. Yang, J.S. Temenoff, Engineering orthopedic tissue interfaces, Tissue Eng. B Rev. 15 (2009) 127–141, https://doi.org/10.1089/ten.teb.2008.0371.
[70] N.T. Tran, Y.K. Kim, S.Y. Kim, M.H. Lee, K.B. Lee, Comparative osteogenesis and degradation behavior of magnesium implant in epiphysis and diaphysis of the long bone in the rat model, Materials 15 (2022), https://doi.org/10.3390/ma15165630.
[71] P. Han, M. Tan, S. Zhang, W. Ji, J. Li, X. Zhang, C. Zhao, Y. Zheng, Y. Chai, Shape and site dependent in vivo degradation of Mg-Zn pins in rabbit femoral condyle, Int. J. Mol. Sci. 15 (2014) 2959–2970, https://doi.org/10.3390/ijms15022959.
[72] I. Puigdomenech, Chemical Equilibrium Diagrams, 2020 n.d.), https://www.kth.se/ch%0De/medusa/chemeq-1.369367.
[73] Anon, Standard Practice for Preparing, Cleaning, and Evaluating Corrosion Test Specimens, ASTM Spec. Tech. Publ. i, 2017, pp. 505–510, https://doi.org/10.1520/G0001-03R17E01.2.
[74] E.P. Shubhakar Nidadavolu, F. Feyerabend, T. Ebel, R. Willumeit-Römer, M. Dahms, On the determination of magnesium degradation rates under physiological conditions, Materials 9 (2016) 1–10, https://doi.org/10.3390/ma9080627.
[75] B. Zeller-Plumhoff, M. Gile, M. Priebe, H. Slominska, B. Boll, B. Wiese, T. Würger, R. Willumeit-Römer, R.H. Meißner, Exploring key ionic interactions for magnesium degradation in simulated body fluid – a data-driven approach, Corrosion Sci. 182 (2021), https://doi.org/10.1016/j.corsci.2021.109272.
[76] J. Schindelin, I. Arganda-Carreras, E. Frise, V. Kaynig, M. Longair, T. Pietzsch, S. Preibisch, C. Rueden, S. Saalfeld, B. Schmid, J.-Y. Tinevez, D.J. White, V. Hartenstein, K. Eliceiri, P. Tomancak, A. Cardona, Fiji: an open-source platform for biological-image analysis, Nat. Methods 9 (2012) 676–682, https://doi.org/10.1038/nmeth.2019.
[77] W.H. Ma, Y.J. Liu, W. Wang, Y.Z. Zhang, Improved biological performance of magnesium by micro-arc oxidation, Braz. J. Med. Biol. Res. 48 (2015) 214–225, https://doi.org/10.1590/1414-431X20144171.
[78] Y. Xin, K. Huo, T. Hu, G. Tang, P.K. Chu, Corrosion products on biomedical magnesium alloy soaked in simulated body fluids, J. Mater. Res. 24 (2009) 2711–2719, https://doi.org/10.1557/jmr.2009.0323.
[79] J. Lévesque, H. Hermawan, D. Dubé, D. Mantovani, Design of a pseudo-physiological test bench specific to the development of biodegradable metallic

biomaterials, Acta Biomater. 4 (2008) 284–295, https://doi.org/10.1016/j.actbio.2007.09.012.
[80] K. Iskhakova, D.C. Florian Wieland, R. Marek, U. Schwarze, A. Davydok, H. Cwieka, T. AlBaraghtheh, J. Reimers, B. Hindenlang, S. Sefa, R. Willumeit-Römer, B. Zeller-Plumhoff, Sheep Bone Ultrastructure Analyses Reveal Differences in Bone Maturation Around Mg-Based and Ti Implants, ((n.d.)).
[81] E. Willbold, F. Witte, Histology and research at the hard tissue-implant interface using Technovit 9100 New embedding technique, Acta Biomater. 6 (2010) 4447–4455, https://doi.org/10.1016/j.actbio.2010.06.022.
[82] P. Thévenaz, M. Unser, User-friendly semiautomated assembly of accurate image mosaics in microscopy, Microsc. Res. Tech. 70 (2007) 135–146, https://doi.org/10.1002/jemt.20393.
[83] C. Kunert-Keil, H. Richter, I. Zeidler-Rentzsch, I. Bleeker, T. Gredes, Histological comparison between laser microtome sections and ground specimens of implant-containing tissues, Ann. Anat. 222 (2019) 153–157, https://doi.org/10.1016/j.aanat.2018.12.001.
[84] T. Albrektsson, A. Wennerberg, Oral implant surfaces: Part 1–review focusing on topographic and chemical properties of different surfaces and in vivo responses to them, Int. J. Prosthodont. (IJP) 17 (2004) 536–543.
[85] S. Farahany, H.R. Bakhsheshi-Rad, M.H. Idris, M.R. Abdul Kadir, A.F. Lotfabadi, A. Ourdjini, In-situ thermal analysis and macroscopical characterization of Mg-xCa and Mg-0.5Ca-xZn alloy systems, Thermochim. Acta 527 (2012) 180–189, https://doi.org/10.1016/j.tca.2011.10.027.
[86] A. Dobkowska, B. Adamczyk-Cieślak, M. Chlewicka, A. Towarek, A. Zielińska, M. Koralnik, D. Kuc, J. Mizera, Evolution of microstructure dependent corrosion properties of ultrafine AZ31 under conditions of extrusion with a forward backward oscillating die, J. Mater. Res. Technol. 18 (2022) 4486–4496, https://doi.org/10.1016/j.jmrt.2022.04.131.
[87] A. Dobkowska, B. Adamczyk – Cieślak, D. Kuc, E. Hadasik, T. Płociński, E. Ura-Bińczyk, J. Mizera, Influence of bimodal grain size distribution on the corrosion resistance of Mg–4Li–3Al–1Zn (Laz431), J. Mater. Res. Technol. 13 (2021) 346–358, https://doi.org/10.1016/j.jmrt.2021.04.078.
[88] A. Tripathi, S.V.S.N. Murty, P.R. Narayanan, Microstructure and texture evolution in AZ31 magnesium alloy during caliber rolling at different temperatures, J. Magnesium Alloys 5 (2017) 340–347, https://doi.org/10.1016/j.jma.2017.07.001.
[89] J. Gonzalez, R.Q. Hou, E.P.S. Nidadavolu, R. Willumeit-Römer, F. Feyerabend, Magnesium degradation under physiological conditions – best practice, Bioact. Mater. 3 (2018) 174–185, https://doi.org/10.1016/j.bioactmat.2018.01.003.
[90] N.A. Agha, R. Willumeit-Romer, D. Laipple, B. Luthringer, F. Feyerabend, The degradation interface of magnesium based alloys in direct contact with human primary osteoblast cells, PLoS One 11 (2016), https://doi.org/10.1371/journal.pone.0157874.
[91] N.T.H. Farr, G.M. Hughes, C. Rodenburg, Monitoring carbon in electron and ion beam deposition within fib-sem, Materials 14 (2021), https://doi.org/10.3390/ma14113034.
[92] Z. Li, G.L. Song, S. Song, Effect of bicarbonate on biodegradation behaviour of pure magnesium in a simulated body fluid, Electrochim. Acta 115 (2014) 56–65, https://doi.org/10.1016/J.ELECTACTA.2013.10.131.
[93] T.A. Mahmood, J.E. Davies, Incorporation of amino acids within the surface reactive layers of bioactive glass in vitro: an XPS study, J. Mater. Sci. Mater. Med. 11 (2000) 19–23, https://doi.org/10.1023/A:1008929500904/METRICS.
[94] A. Shchukarev, B.Ö. Malekzadeh, M. Ransjö, P. Tengvall, A. Westerlund, Surface characterization of insulin-coated Ti6Al4V medical implants conditioned in cell culture medium: an XPS study, J. Electron. Spectrosc. Relat. Phenom. 216 (2017) 33–38, https://doi.org/10.1016/J.ELSPEC.2017.03.001.
[95] F.X. Qin, C. Ji, Z.H. Dan, G.Q. Xie, H. Wang, S.I. Yamaura, M. Niinomi, Y. De Li, Corrosion behavior of MgZnCa bulk amorphous alloys fabricated by spark plasma sintering, Acta Metall. Sin. (English Lett. 29 (2016) 793–799, https://doi.org/10.1007/S40195-016-0451-9/FIGURES/7.
[96] D.L. Felker, P.M.A. Sherwood, Magnesium phosphate (Mg3(PO4) 2) by XPS, Surf. Sci. Spectra 9 (2021) 83, https://doi.org/10.1116/11.20030104.
[97] A. Dobkowska, B. Adamczyk – Cieślak, J. Kubásek, D. Vojtěch, D. Kuc, E. Hadasik, J. Mizera, Microstructure and corrosion resistance of a duplex structured Mg–7.5Li–3Al–1Zn, J. Magnesium Alloys 9 (2021) 467–477, https://doi.org/10.1016/j.jma.2020.07.007.
[98] A. Atrens, Z. Shi, S.U. Mehreen, S. Johnston, G.L. Song, X. Chen, F. Pan, Review of Mg alloy corrosion rates, J. Magnesium Alloys 8 (2020) 989–998, https://doi.org/10.1016/j.jma.2020.08.002.
[99] Z. Shi, M. Liu, A. Atrens, Measurement of the corrosion rate of magnesium alloys using Tafel extrapolation, Corrosion Sci. 52 (2010) 579–588, https://doi.org/10.1016/j.corsci.2009.10.016.
[100] H.R. Bakhsheshi-Rad, M.H. Idris, M.R. Abdul-Kadir, A. Ourdjini, M. Medraj, M. Daroonparvar, E. Hamzah, Mechanical and bio-corrosion properties of quaternary Mg-Ca-Mn-Zn alloys compared with binary Mg-Ca alloys, Mater. Des. 53 (2014) 283–292, https://doi.org/10.1016/j.matdes.2013.06.055.
[101] W.A. Badawy, N.H. Hilal, M. El-Rabiee, H. Nady, Electrochemical behavior of Mg and some Mg alloys in aqueous solutions of different pH, Electrochim. Acta 55 (2010) 1880–1887, https://doi.org/10.1016/j.electacta.2009.10.083.
[102] A.D. King, N. Birbilis, J.R. Scully, Accurate electrochemical measurement of magnesium corrosion rates; A combined impedance, mass-loss and hydrogen collection study, Electrochim. Acta 121 (2014) 394–406, https://doi.org/10.1016/j.electacta.2013.12.124.
[103] S. Leleu, B. Rives, N. Causse, N. Pébère, Corrosion rate determination of rare-earth Mg alloys in a Na2SO4 solution by electrochemical measurements and inductive coupled plasma-optical emission spectroscopy, J. Magnesium Alloys 7 (2019) 47–57, https://doi.org/10.1016/j.jma.2018.12.002.
[104] P. Brunner, F. Brumbauer, S. Eva-Maria, O. Renk, A.-Ma Weinberg, H. Schroettner, R. Wurchum, Influence of high-pressure torsion deformation on the corrosion behaviour of a bioresorbable Mg-based alloy studied by positron annihilation, Biomater. Sci. 9 (2021) 4099–4109, https://doi.org/10.1039/D1BM00166C.
[105] M. Ascencio, M. Pekguleryuz, S. Omanovic, An investigation of the corrosion mechanisms of WE43 Mg alloy in a modified simulated body fluid solution: the influence of immersion time, Corrosion Sci. 87 (2014) 489–503, https://doi.org/10.1016/j.corsci.2014.07.015.
[106] N.I. Zainal Abidin, A.D. Atrens, D. Martin, A. Atrens, Corrosion of high purity Mg, Mg2Zn0.2Mn, ZE41 and AZ91 in Hank's solution at 37°C, Corrosion Sci. 53 (2011) 3542–3556, https://doi.org/10.1016/j.corsci.2011.06.030.
[107] I. Antoniac, R. Adam, A. Biță, M. Miculescu, O. Trante, I.M. Petrescu, M. Pogărăşteanu, Comparative assessment of in vitro and in vivo biodegradation of Mg-1Ca magnesium alloys for orthopedic applications, Materials 14 (2021) 1–20, https://doi.org/10.3390/ma14010084.
[108] Y. Wen, Q. Liu, J. Wang, Q. Yang, W. Zhao, B. Qiao, Y. Li, D. Jiang, Improving in vitro and in vivo corrosion resistance and biocompatibility of Mg–1Zn–1Sn alloys by microalloying with Sr, Bioact. Mater. 6 (2021) 4654–4669, https://doi.org/10.1016/j.bioactmat.2021.04.043.
[109] H. Xu, T. Hu, M. Wang, Y. Zheng, H. Qin, H. Cao, Z. An, Degradability and biocompatibility of magnesium-MAO: the consistency and contradiction between in-vitro and in-vivo outcomes, Arab. J. Chem. 13 (2020) 2795–2805, https://doi.org/10.1016/j.arabjc.2018.07.010.
[110] E. Bonyadi Rad, S. Mostofi, M. Katschnig, P. Schmutz, M. Pawelkiewicz, R. Willumeit-Römer, U. Schäfer, A. Weinberg, Differential apoptotic response of MC3T3-E1 pre-osteoblasts to biodegradable magnesium alloys in an in vitro direct culture model, J. Mater. Sci. Mater. Med. 28 (2017), https://doi.org/10.1007/s10856-017-5969-5.
[111] G. Baril, N. Pébère, Corrosion of pure magnesium in aerated and deaerated sodium sulphate solutions, Corrosion Sci. 43 (2001) 471–484, https://doi.org/10.1016/S0010-938X(00)00095-0.
[112] T.L. Nguyen, A. Blanquet, M.P. Staiger, G.J. Dias, T.B.F. Woodfield, On the role of surface roughness in the corrosion of pure magnesium in vitro, J. Biomed. Mater. Res. Part B Appl. Biomater. 100 B (2012) 1310–1318, https://doi.org/10.1002/jbm.b.32697.
[113] N. Zhao, D. Zhu, Collagen self-assembly on orthopedic magnesium biomaterials surface and subsequent bone cell attachment, PLoS One 9 (2014), https://doi.org/10.1371/journal.pone.0110420.
[114] S.A. Rowland, S.W. Shalaby, R.A. Latour, A.F. von Recum, Effectiveness of cleaning surgical implants: quantitative analysis of contaminant removal, J. Appl. Biomater. 6 (1995), https://doi.org/10.1002/jab.770060102.
[115] D.U. Duddeck, T. Albrektsson, A. Wennerberg, C. Larsson, F. Beuer, On the cleanliness of different oral implant systems: a pilot study, J. Clin. Med. 8 (2019), https://doi.org/10.3390/jcm8091280.
[116] ISO, Implants for Surgery - Cleanliness of Orthopedic Implants - General Requirements, 2018. ISO 19227:2018).
[117] H. Lu, L. Zhou, L. Wan, S. Li, M. Rong, Z. Guo, Effects of storage methods on time-related changes of titanium surface properties and cellular response, Biomed. Mater. 7 (2012), https://doi.org/10.1088/1748-6041/7/5/055002.
[118] H. Ibrahim, A.D. Klarner, B. Poorganji, D. Dean, A.A. Luo, M. Elahinia, Microstructural, mechanical and corrosion characteristics of heat-treated Mg-1.2Zn-0.5Ca (wt%) alloy for use as resorbable bone fixation material, J. Mech. Behav. Biomed. Mater. 69 (2017) 203–212, https://doi.org/10.1016/j.jmbbm.2017.01.005.
[119] B. Zeller-Plumhoff, T. AlBaraghtheh, D. Höche, R. Willumeit-Römer, Computational modelling of magnesium degradation in simulated body fluid under physiological conditions, J. Magnesium Alloys 10 (2022) 965–978, https://doi.org/10.1016/j.jma.2021.11.014.
[120] Y.F. Zheng, X.N. Gu, F. Witte, Biodegradable metals, Mater. Sci. Eng. R Rep. 77 (2014) 1–34, https://doi.org/10.1016/j.mser.2014.01.001.
[121] C. Zhang, J. Lin, N.Y.T. Nguyen, Y. Guo, C. Xu, C. Seo, E. Villafana, H. Jimenez, Y. Chai, R. Guan, H. Liu, Antimicrobial bioresorbable Mg-Zn-Ca alloy for bone repair in a comparison study with Mg-Zn-Sr alloy and pure Mg, ACS Biomater. Sci. Eng. 6 (2020) 517–538, https://doi.org/10.1021/acsbiomaterials.9b00903.
[122] S.V. Lamaka, J. Gonzalez, D. Mei, F. Feyerabend, R. Willumeit-Römer, M. L. Zheludkevich, Local pH and its evolution near Mg alloy surfaces exposed to simulated body fluids, Adv. Mater. Interfac. 5 (2018) 1–6, https://doi.org/10.1002/admi.201800169.
[123] A. Modabber, D. Zander, N. Zumdick, D. Schick, K. Kniha, S.C. Möhlhenrich, F. Hölzle, E. Goloborodko, Impact of wound closure on the corrosion rate of biodegradable mg-ca-zn alloys in the oral environment, Materials 13 (2020) 1–11, https://doi.org/10.3390/MA13194226.
[124] H.R. Bakhsheshi-Rad, M.R. Abdul-Kadir, M.H. Idris, S. Farahany, Relationship between the corrosion behavior and the thermal characteristics and microstructure of Mg-0.5Ca-xZn alloys, Corrosion Sci. 64 (2012) 184–197, https://doi.org/10.1016/j.corsci.2012.07.015.
[125] H.R. Bakhsheshi-Rad, E. Hamzah, A. Fereidouni-Lotfabadi, M. Daroonparvar, M. A.M. Yajid, M. Mezbahul-Islam, M. Kasiri-Asgarani, M. Medraj, Microstructure and bio-corrosion behavior of Mg-Zn and Mg-Zn-Ca alloys for biomedical applications, Mater. Corros. 65 (2014) 1178–1187, https://doi.org/10.1002/maco.201307588.

[126] D. Zander, N.A. Zumdick, Influence of Ca and Zn on the microstructure and corrosion of biodegradable Mg-Ca-Zn alloys, Corrosion Sci. 93 (2015) 222–233, https://doi.org/10.1016/j.corsci.2015.01.027.
[127] J. Walker, S. Shadanbaz, N.T. Kirkland, E. Stace, T. Woodfield, M.P. Staiger, G. J. Dias, Magnesium alloys: predicting in vivo corrosion with in vitro immersion testing, J. Biomed. Mater. Res. Part B-Applied Biomater. 100B (2012) 1134–1141, https://doi.org/10.1002/jbm.b.32680.
[128] R.A. Lindtner, C. Castellani, S. Tangl, G. Zanoni, P. Hausbrandt, E.K. Tschegg, S. E. Stanzl-Tschegg, A.M. Weinberg, Comparative biomechanical and radiological characterization of osseointegration of a biodegradable magnesium alloy pin and a copolymeric control for osteosynthesis, J. Mech. Behav. Biomed. Mater. 28 (2013) 232–243, https://doi.org/10.1016/j.jmbbm.2013.08.008.
[129] H. Ben, D.C. Martinez, F.A. Shah, A. Johansson, L. Emanuelsson, B. Norlindh, R. Willumeit-r, W. Swieszkowski, A. Palmquist, O. Omar, P. Thomsen, Bioactive Materials Magnesium implant degradation provides immunomodulatory and proangiogenic effects and attenuates peri-implant fibrosis in soft tissues 26 (2023) 353–369, https://doi.org/10.1016/j.bioactmat.2023.02.014.
[130] P. Kolar, K. Schmidt-Bleek, H. Schell, T. Gaber, D. Toben, G. Schmidmaier, C. Perka, F. Buttgereit, G.N. Duda, The early fracture hematoma and its potential role in fracture healing, Tissue Eng. B Rev. 16 (2010) 427–434, https://doi.org/10.1089/ten.teb.2009.0687.
[131] H. Schell, G.N. Duda, A. Peters, S. Tsitsilonis, K.A. Johnson, K. Schmidt-Bleek, The haematoma and its role in bone healing, J. Exp. Orthop. 4 (2017), https://doi.org/10.1186/s40634-017-0079-3.
[132] D.T. Chou, D. Hong, S. Oksuz, R. Schweizer, A. Roy, B. Lee, P. Shridhar, V. Gorantla, P.N. Kumta, Corrosion and bone healing of Mg-Y-Zn-Zr-Ca alloy implants: comparative in vivo study in a non-immobilized rat femoral fracture model, J. Biomater. Appl. 33 (2019) 1178–1194, https://doi.org/10.1177/0885328219825568.
[133] E. Willbold, A.A. Kaya, R.A. Kaya, F. Beckmann, F. Witte, Corrosion of magnesium alloy AZ31 screws is dependent on the implantation site, Mater. Sci. Eng. B Solid-State Mater. Adv. Technol. 176 (2011) 1835–1840, https://doi.org/10.1016/j.mseb.2011.02.010.
[134] E.L. Zhang, L.P. Xu, G.N. Yu, F. Pan, K. Yang, In vivo evaluation of biodegradable magnesium alloy bone implant in the first 6 months implantation, J. Biomed. Mater. Res., Part A 90A (2009) 882–893, https://doi.org/10.1002/jbm.a.32132.
[135] N. Erdmann, N. Angrisani, J. Reifenrath, A. Lucas, F. Thorey, D. Bormann, A. Meyer-Lindenberg, Biomechanical testing and degradation analysis of MgCa0.8 alloy screws: a comparative in vivo study in rabbits, Acta Biomater. 7 (2011) 1421–1428, https://doi.org/10.1016/j.actbio.2010.10.031.
[136] X.N. Gu, X.H. Xie, N. Li, Y.F. Zheng, L. Qin, In vitro and in vivo studies on a Mg-Sr binary alloy system developed as a new kind of biodegradable metal, Acta Biomater. 8 (2012) 2360–2374, https://doi.org/10.1016/j.actbio.2012.02.018.
[137] F. Amerstorfer, S.F. Fischerauer, L. Fischer, J. Eichler, J. Draxler, A. Zitek, M. Meischel, E. Martinelli, T. Kraus, S. Hann, S.E. Stanzl-Tschegg, P. J. Uggowitzer, J.F. Löffler, A.M. Weinberg, T. Prohaska, Long-term in vivo degradation behavior and near-implant distribution of resorbed elements for magnesium alloys WZ21 and ZX50, Acta Biomater. 42 (2016) 440–450, https://doi.org/10.1016/j.actbio.2016.06.025.
[138] A. Karacs, A. Joob Fancsaly, T. Divinyi, G. Peto, G. Kovách, Morphological and animal study of titanium dental implant surface induced by blasting and high intensity pulsed Nd-glass laser, Mater. Sci. Eng. C 23 (2003) 431–435, https://doi.org/10.1016/S0928-4931(02)00316-8.
[139] T. Imwinkelried, S. Beck, T. Iizuka, B. Schaller, Effect of a plasmaelectrolytic coating on the strength retention of in vivo and in vitro degraded magnesium implants, Acta Biomater. 9 (2013) 8643–8649, https://doi.org/10.1016/j.actbio.2012.08.047.
[140] A. Krause, N. von der Hoh, D. Bormann, C. Krause, F.W. Bach, H. Windhagen, A. Meyer-Lindenberg, Degradation behaviour and mechanical properties of magnesium implants in rabbit tibiae, J. Mater. Sci. 45 (2010) 624–632, https://doi.org/10.1007/s10853-009-3936-3.
[141] X.M. Guan, M.P. Xiong, F.Y. Zeng, B. Xu, L.D. Yang, H. Guo, J.L. Niu, J. Zhang, C. X. Chen, J. Pei, H. Huang, G.Y. Yuan, Enhancement of osteogenesis and biodegradation control by brushite coating on Mg-Nd-Zn-Zr alloy for mandibular bone repair, ACS Appl. Mater. Interfaces 6 (2014) 21525–21533, https://doi.org/10.1021/am506543a.
[142] J. Niu, M. Xiong, X. Guan, J. Zhang, H. Huang, J. Pei, G. Yuan, The in vivo degradation and bone-implant interface of Mg-Nd-Zn-Zr alloy screws: 18 months post-operation results, Corrosion Sci. 113 (2016) 183–187, https://doi.org/10.1016/J.CORSCI.2016.10.009.
[143] M. Ma, D.B. Pokharel, J. Dong, L. Wu, R. Zhao, Y. Zhu, J. Hou, J. Xie, S. Sui, C. Wang, W. Ke, In vivo corrosion behavior of pure magnesium in femur bone of rabbit, J. Alloys Compd. 848 (2020), 156506, https://doi.org/10.1016/j.jallcom.2020.156506.
[144] L.L. Tan, Q. Wang, X. Lin, P. Wan, G.D. Zhang, Q. Zhang, K. Yang, Loss of mechanical properties in vivo and bone-implant interface strength of AZ31B magnesium alloy screws with Si-containing coating, Acta Biomater. 10 (2014) 2333–2340, https://doi.org/10.1016/j.actbio.2013.12.020.
[145] L. Tätting, O. Sandberg, M. Bernhardsson, J. Ernerudh, P. Aspenberg, Different composition of leucocytes in cortical and cancellous bone healing in a mouse model, Bone Jt. Res. 7 (2018) 620–628, https://doi.org/10.1302/2046-3758.712.BJR-2017-0366.R2.
[146] L. Quintens, M. Herteleer, S. Vancleef, Y. Carette, J. Duflou, S. Nijs, J. Vander Sloten, H. Hoekstra, Anatomical variation of the tibia – a principal component analysis, Sci. Rep. 9 (2019) 1–10, https://doi.org/10.1038/s41598-019-44092-8.
[147] D. Dimitriou, T.Y. Tsai, B. Yue, H.E. Rubash, Y.M. Kwon, G. Li, Side-to-side variation in normal femoral morphology: 3D CT analysis of 122 femurs 102 (2016) 91–97, https://doi.org/10.1016/j.otsr.2015.11.004.
[148] N.S. Martynenko, N.Y. Anisimova, O.V. Rybalchenko, M.V. Kiselevskiy, G. Rybalchenko, B. Straumal, D. Temralieva, A.T. Mansharipova, A.O. Kabiyeva, M.T. Gabdullin, S. Dobatkin, Y. Estrin, Rationale for processing of a mg-zn-ca alloy by equal-channel angular pressing for use in biodegradable implants for osteoreconstruction, Crystals (2021) 11, https://doi.org/10.3390/cryst11111381.
[149] M.S. Dargusch, N. Balasubramani, N. Yang, S. Johnston, Y. Ali, G. Wang, J. Venezuela, J. Carluccio, C. Lau, R. Allavena, D. Liang, K. Mardon, Q. Ye, In vivo performance of a rare earth free Mg–Zn–Ca alloy manufactured using twin roll casting for potential applications in the cranial and maxillofacial fixation devices, Bioact. Mater. 12 (2022) 85–96, https://doi.org/10.1016/j.bioactmat.2021.10.026.
[150] F. Witte, J. Fischer, J. Nellesen, C. Vogt, J. Vogt, T. Donath, F. Beckmann, In vivo corrosion and corrosion protection of magnesium alloy LAE442, Acta Biomater. 6 (2010) 1792–1799, https://doi.org/10.1016/j.actbio.2009.10.012.
[151] D. Zhao, T. Wang, K. Nahan, X. Guo, Z. Zhang, Z. Dong, S. Chen, D.T. Chou, D. Hong, P.N. Kumta, W.R. Heineman, In vivo characterization of magnesium alloy biodegradation using electrochemical H2 monitoring, ICP-MS, and XPS, Acta Biomater. 50 (2017) 556–565, https://doi.org/10.1016/j.actbio.2017.01.024.
[152] R.A. Kaya, H. Cavusoglu, C. Tanik, A.A. Kaya, O. Duygulu, Z. Mutlu, E. Zengin, Y. Aydin, The effects of magnesium particles in posterolateral spinal fusion: an experimental in vivo study in a sheep model, J. Neurosurg. Spine 6 (2007) 141–149, https://doi.org/10.3171/spi.2007.6.2.141.
[153] P.P. Lelovas, T.T. Xanthos, S.E. Thorma, G.P. Lyritis, I.A. Dontas, The laboratory rat as an animal model for osteoporosis research, Comp. Med. 58 (2008) 424–430.
[154] G. Osterhoff, E.F. Morgan, S.J. Shefelbine, L. Karim, L.M. McNamara, P. Augat, Bone mechanical properties and changes with osteoporosis, Injury 47 (2016), https://doi.org/10.1016/S0020-1383(16)47003-8. S11–S20.
[155] S.Y. Cho, S.W. Chae, K.W. Choi, H.K. Seok, H.S. Han, S.J. Yang, Y.Y. Kim, J. T. Kim, J.Y. Jung, M. Assad, Load-bearing capacity and biological allowable limit of biodegradable metal based on degradation rate in vivo, J. Biomed. Mater. Res. Part B Appl. Biomater. 100 B (2012) 1535–1544, https://doi.org/10.1002/jbm.b.32722.
[156] J. Kuhlmann, I. Bartsch, E. Willbold, S. Schuchardt, O. Holz, N. Hort, D. Höche, W.R. Heineman, F. Witte, Fast escape of hydrogen from gas cavities around corroding magnesium implants, Acta Biomater. 9 (2013) 8714–8721, https://doi.org/10.1016/j.actbio.2012.10.008.
[157] J. Wang, H. Jiang, Y. Bi, J.E. Sun, M. Chen, D. Liu, Effects of gas produced by degradation of Mg-Zn-Zr Alloy on cancellous bone tissue, Mater. Sci. Eng. C 55 (2015) 556–561, https://doi.org/10.1016/j.msec.2015.05.082.
[158] U. Thormann, V. Alt, L. Heimann, C. Gasquere, C. Heiss, G. Szalay, J. Franke, R. Schnettler, K.S. Lips, The biocompatibility of degradable magnesium interference screws: an experimental study with sheep, BioMed Res. Int. 2015 (2015), https://doi.org/10.1155/2015/943603.
[159] A. Yamamoto, A. Kikuta, Development of a model system for gas cavity formation behavior of magnesium alloy implantation, ACS Biomater. Sci. Eng. 8 (2022) 2437–2444, https://doi.org/10.1021/acsbiomaterials.1c01429.
[160] M. Thomann, C. Krause, D. Bormann, N. Von Der Höh, H. Windhagen, A. Meyer-Lindenberg, N. von der Hoh, H. Windhagen, A. Meyer-Lindenberg, Comparison of the resorbable magnesium alloys LAE442 und MgCa0.8 concerning their mechanical properties, their progress of degradation and the bone-implant-contact after 12 months implantation duration in a rabbit model, Mater. Werkst. 40 (2009) 82–87, https://doi.org/10.1002/mawe.200800412.
[161] D. Bian, J. Deng, N. Li, X. Chu, Y. Liu, W. Li, H. Cai, P. Xiu, Y. Zhang, Z. Guan, Y. Zheng, Y. Kou, B. Jiang, R. Chen, In vitro and in vivo studies on biomedical magnesium low-alloying with elements gadolinium and zinc for orthopedic implant applications, ACS Appl. Mater. Interfaces 10 (2018) 4394–4408, https://doi.org/10.1021/acsami.7b15498.